

Comparison of Simulated Polarimetric Signatures in Idealized Supercell Storms Using Two-Moment Bulk Microphysics Schemes in WRF

MARCUS JOHNSON

Center for Analysis and Prediction of Storms, and School of Meteorology, University of Oklahoma, Norman, Oklahoma

YOUNGSUN JUNG AND DANIEL T. DAWSON II

Center for Analysis and Prediction of Storms, University of Oklahoma, Norman, Oklahoma

MING XUE

Center for Analysis and Prediction of Storms, and School of Meteorology, University of Oklahoma, Norman, Oklahoma

(Manuscript received 23 June 2015, in final form 2 December 2015)

ABSTRACT

Microphysics parameterization becomes increasingly important as the model grid spacing increases toward convection-resolving scales. The performance of several partially or fully two-moment (2M) schemes within the Weather Research and Forecasting (WRF) Model, version 3.5.1, chosen because of their well-documented advantages over one-moment (1M) schemes, is evaluated with respect to their ability in producing the well-known polarimetric radar signatures found within supercell storms. Such signatures include the Z_{DR} and K_{DP} columns, the Z_{DR} arc, the midlevel Z_{DR} and ρ_{HV} rings, the hail signature in the forward-flank downdraft, and the K_{DP} foot. Polarimetric variables are computed from WRF Model output using a polarimetric radar simulator. It is found that microphysics schemes with a 1M rimed-ice category are unable to simulate the Z_{DR} arc, despite containing a 2M rain category. It is also found that a hail-like rimed-ice category (in addition to graupel) may be necessary to reproduce the observed hail signature. For the microphysics schemes that only contain a graupel-like rimed-ice category, only very wet graupel particles are able to reach the lowest model level, which did not adequately reduce Z_{DR} in this signature. The most realistic signatures overall are found with microphysics schemes that are fully 2M with a separate hail category.

1. Introduction

Realistic simulations of supercell storm structure and precipitation rely heavily on accurate treatment of cloud and precipitation microphysical processes. The two main approaches of modeling those processes employ 1) spectral bin (e.g., [Khain et al. 2004](#)) and 2) bulk microphysics parameterization (BMP) schemes (e.g., [Lin et al. 1983](#); [Milbrandt and Yau 2005a,b](#), hereafter [MY05a](#) and [MY05b](#), respectively). The spectral bin scheme is generally more flexible because the hydrometeor particle size distribution (PSD) is discretized into bins commonly sorted by mass or

diameter and explicitly predicted without assuming an underlying functional form, but bin schemes are computationally very expensive. For this reason, BMP schemes are used almost exclusively in real-time forecasts where microphysics parameterization is needed. BMP schemes typically assume a functional form of the PSD [although at least one BMP scheme predicts moments related to observed variables without an underlying PSD, see [Kogan and Belochitski \(2012\)](#)]. The most commonly assumed PSD function is the gamma distribution:

$$N(D) = N_0 D^\alpha \exp(-\Lambda D), \quad (1)$$

where N_0 , Λ , and α are the intercept, slope, and shape parameters, respectively, of the gamma distribution while D is the particle diameter. With the gamma PSD, physical quantities such as mixing ratio and total number concentration can be related to various moments of

Corresponding author address: Youngsun Jung, CAPS, University of Oklahoma, NWC Suite 2500, 120 David Boren Blvd., Norman, OK 73072.
E-mail: youngsun.jung@ou.edu

the PSD. Specifically, the n th moment of the gamma PSD is given by the following equation:

$$M(n) = \int_0^{\infty} D^n N(D) dD = \frac{N_0 \Gamma(\alpha + n + 1)}{\Lambda^{\alpha + n + 1}}, \quad (2)$$

where $\Gamma(n)$ is the gamma function.

Accordingly, microphysics schemes are commonly referred to by the number of distinct moments they predict for a given hydrometeor category [i.e., a scheme that predicts one moment of the PSD is a single-moment/one-moment (1M) scheme]. The 1M microphysics schemes usually predict mass mixing ratio q , which is proportional to the third moment for spherical hydrometeors (e.g., Kessler 1969; Lin et al. 1983; Rutledge and Hobbs 1983; Tao and Simpson 1993; Straka and Mansell 2005). Typically, double-moment (2M) schemes additionally predict total number concentration N_t (the zeroth moment), though the number of hydrometeor categories with predicted N_t varies by scheme (e.g., Ziegler 1985; Cotton et al. 1986; Ferrier 1994; Meyers et al. 1997; Cohard and Pinty 2000; Thompson et al. 2008; Morrison et al. 2009; Mansell et al. 2010). Triple-moment (3M) schemes that additionally predict the radar reflectivity factor Z (proportional to the sixth moment) have also been developed [Milbrandt–Yau (MY3): MY05a and MY05b; Ziegler Variable Density (ZVD): Dawson et al. (2014, hereafter D14)], which carry an increased computational cost with the additional predicted moment.

Multimoment microphysics schemes that predict two or more moments consistently outperform 1M schemes in convective storm simulations. Specifically, recent studies (Milbrandt and Yau 2006; Dawson et al. 2010, 2015b) produced better storm structure and cold pool characteristics using the 2M and 3M versions of the MY05a–MY05b scheme than the 1M version. Additional studies (e.g., Wacker and Seifert 2001; MY05a; Dawson et al. 2010; Jung et al. 2010a, hereafter J10a; Milbrandt and McTaggart-Cowan 2010) have shown that sedimentation in 1M schemes lacks a size-sorting effect, owing to the use of a single-moment-weighted fall speed for the entire distribution of a given hydrometeor. Size sorting is a fundamental microphysical mechanism and one that is particularly important in supercell thunderstorms (e.g., Kumjian and Ryzhkov 2008, hereafter KR08; Kumjian and Ryzhkov 2009, hereafter KR09; D14; Dawson et al. 2015a). In Jung et al. (2012), the structure and magnitude of analyzed polarimetric variables for a supercell storm were more similar to observations with the use of a 2M scheme than with a 1M scheme. Based on these studies, more recent studies at the convective scale [horizontal grid spacing ≤ 4 km;

Weisman et al. (1997)] are using 2M schemes (e.g., J10a; Dawson et al. 2012; Mansell and Ziegler 2013; Potvin et al. 2013; Putnam et al. 2014).

Radar reflectivity is commonly used to evaluate model performance, but with the increased number of prognostic variables associated with multimoment microphysics schemes and often additional hydrometeor types, reflectivity alone becomes insufficient (Jung et al. 2010b; Xue et al. 2010b). Polarimetric radar variables can be very useful because they can provide additional information on the size distribution, total amount, phase, and type of hydrometeors present. Briefly, differential reflectivity Z_{DR} is the ratio of return power at horizontal and vertical polarizations, and is related to the shape of scatterers. The cross-correlation coefficient ρ_{HV} is the correlation of horizontally and vertically polarized pulses within the radar resolution volume and is influenced by the complexity of the scatterer's shape and phase composition. Finally, specific differential phase K_{DP} is the difference of phase shift between the horizontally and vertically polarized pulses traveling through a medium over a given distance, and is sensitive to the mass of the medium (e.g., rain, hail, etc.).

This study attempts to gain understanding of the difference in the behaviors of several microphysics schemes available in the Weather Research and Forecasting (WRF) Model (Skamarock et al. 2008) by examining simulated polarimetric radar variables and comparing hydrometeor frequency distributions between the microphysics schemes. We focus on the 2M (partially or fully) schemes available within WRF (version 3.5.1). Such simulations and comparisons can be especially useful to model developers to help them understand the behaviors of microphysics parameterization schemes. For example, recent studies (e.g., J10a; Kumjian and Ryzhkov 2012; D14) have used simulated radar observations to show the performance of microphysics schemes depending on the predicted moments. Synthetic satellite observations are also used to help understand and improve some microphysics schemes (e.g., Cintineo et al. 2014).

An idealized supercell thunderstorm is chosen for this study because of the prominent and well-documented polarimetric signatures present in such storms. In this paper, we focus on the Z_{DR} and K_{DP} columns, Z_{DR} arc, midlevel Z_{DR} and ρ_{HV} rings, hail signature in the forward-flank downdraft, and K_{DP} foot in simulated supercells following J10a. Briefly, the Z_{DR} and K_{DP} columns are regions of enhanced Z_{DR} and K_{DP} associated with strong updrafts. The increase in Z_{DR} is from large oblate raindrops (that can be advected above the melting level) and wet rimed ice, while the increase in K_{DP} is due to water mass from shed raindrops and wet

TABLE 1. Example references of observed polarimetric signatures examined in this paper.

Observed polarimetric signatures	References
Z_{DR} column	Illingworth et al. (1987); Conway and Zrnić (1993); Brandes et al. (1995); Loney et al. (2002)
K_{DP} column	Hubbert et al. (1998); Loney et al. (2002)
Z_{DR} arc	Ryzhkov et al. (2005); Kumjian and Ryzhkov (2008); Kumjian and Ryzhkov (2009)
Midlevel Z_{DR}/ρ_{HV} rings	Kumjian and Ryzhkov (2008)
Hail signature in forward-flank downdraft	Kumjian and Ryzhkov (2008)
K_{DP} foot	Romine et al. (2008)

rimed ice. The Z_{DR} arc is an area of enhanced Z_{DR} near the surface due to size sorting of rimed ice and raindrops, which result in large raindrops (high Z_{DR}) on the southern edge of the right-moving supercell. The Z_{DR} and ρ_{HV} rings are ringlike patterns of enhanced Z_{DR} and depressed ρ_{HV} in the midlevels near the updraft due to large raindrops and wet rimed ice. The hail signature in the forward-flank downdraft is an area of low Z_{DR} near the surface due to dry, tumbling hail. Last, the K_{DP} foot is a region of enhanced K_{DP} near the surface, possibly due to melting hail. For more details of each signature, we refer readers to the references in Table 1. Since these polarimetric signatures are significantly influenced by microphysical processes, the presence and magnitude of each simulated signature provide a basis for evaluating the performance of microphysics schemes and their ability to replicate these processes in simulations. Being able to replicate these processes and signatures is also crucial to direct assimilation of polarimetric radar data into convective-scale NWP models, since the updates to the model state variables by these observations rely on properly simulated linkages between the observed quantities with the model states within the assimilating model. In this paper, we identify and discuss weaknesses and shortcomings in the ability of the microphysics schemes to simulate these signatures.

The rest of the paper is organized as follows. The simulation model configurations and the polarimetric simulator are first discussed in section 2, polarimetric signatures using different microphysics schemes are discussed in section 3, hydrometeor distributions are discussed in section 4, and conclusions are given in section 5.

2. Numerical simulations and polarimetric radar data simulator

a. Model configuration

The WRF Model (v3.5.1) is employed for idealized supercell storm simulations in this study. The model configuration is detailed in Table 2 and is based on that in Morrison and Milbrandt (2011), which also compared

the use of different microphysics schemes (albeit limited to two) in idealized supercell simulations. The horizontal grid spacing is 1 km while the vertical grid spacing is approximately 500 m. No radiation, land surface, cumulus, or planetary boundary layer parameterization schemes are employed for simplicity. The thermodynamic component of the WRF idealized supercell sounding follows Weisman and Klemp (1982). The vertical wind profile contains veering winds with shear of $5.15 \times 10^{-3} \text{ s}^{-1}$ for $z = 0.25\text{--}2.75$ km and unidirectional horizontal shear equal to $5.4 \times 10^{-3} \text{ s}^{-1}$ above for $z = 2.75\text{--}7.25$ km. An ellipsoidal thermal bubble with horizontal and vertical radii of 10 and 1.5 km, respectively, initializes convection with a maximum potential temperature perturbation θ' (with respect to the environmental sounding) of 3 K at the center of the bubble. The bubble is centered at $z = 1.5$ km and in the middle of the horizontal domain. For further details, we refer the reader to Morrison and Milbrandt (2011).

b. Microphysics schemes

In this study, we evaluate five partially or completely 2M schemes in the WRF Model: the Morrison

TABLE 2. WRF Model input.

WRF Model configuration	
Run time	180 min
Δt	6 s
Sound wave Δt	1 s
Model output interval	10 min
Horizontal domain	199 km \times 199 km
Model lid	20 km
Δx	1 km
Δy	1 km
Δz	\sim 500 m
Time integration scheme	Third order Runge–Kutta
Horizontal momentum advection	Fifth order
Vertical momentum advection	Third order
Horizontal scalar advection	Fifth order
Vertical scalar advection	Third order
Upper-level damping	5000 m below model top
Rayleigh damping coefficient	0.003
Horizontal boundary conditions	Open

TABLE 3. Prognostic variables in the microphysics schemes evaluated in this study. Here q denotes mass mixing ratio, N_t denotes total number concentration, and \bar{v} denotes particle volume. A hydrometeor category that is not included in a microphysics scheme is listed as not applicable (NA). In WRF output, the prognostic number concentration is in mixing ratio units (number per kilogram).

	Morrison	MY2	NSSL	Thompson	WDM6
Cloud droplets	q	q, N_t	q, N_t	q	q, N_t
Rain	q, N_t	q, N_t	q, N_t	q, N_t	q, N_t
Cloud ice	q, N_t	q, N_t	q, N_t	q, N_t	q
Snow	q, N_t	q, N_t	q, N_t	q	q
Graupel	q, N_t	q, N_t	q, N_t, \bar{v}	q	q
Hail	NA	q, N_t	q, N_t	NA	NA

(Morrison et al. 2009), Milbrandt–Yau (hereafter MY2 to distinguish from the 1M and 3M versions of the scheme; MY05a, MY05b), National Severe Storms Laboratory (NSSL; Mansell et al. 2010), Thompson (Thompson et al. 2008), and the WRF double-moment 6-class microphysics scheme (WDM6; Lim and Hong 2010). Table 3 lists the hydrometeor categories and variables that each scheme examined in this study predicts. Specifically, the MY2 and NSSL microphysics schemes are fully double-moment (2M) since these schemes each predict mass mixing ratio q and total number concentration N_t for each hydrometeor category. Additionally, these schemes contain a separate hail-like in addition to a graupel-like rimed-ice category. The Morrison, Thompson, and WDM6 schemes only contain a graupel-like rimed-ice category, and the graupel categories in the Thompson and WDM6 schemes are 1M. Further, the WDM6 scheme contains a fixed graupel intercept parameter (Hong and Lim 2006), while the Thompson scheme diagnoses graupel intercept parameter depending on its mixing ratio and the median volume diameter of supercooled rain (Morrison et al. 2015, hereafter M15). We note here that the namelist hail-switch option for the WRF single-moment 6-class (WSM6; Hong and Lim 2006), WDM6, and Morrison microphysics schemes is available from WRF v3.6.1 forward that allows users to choose either graupel-like or hail-like (default option) parameters for the rimed-ice category, but the option is not available in the 3.5.1 version used in this study. Since the Morrison, Thompson, and WDM6 microphysics schemes are 2M for some categories and 1M for others, they are *partially* 2M. Additionally, the NSSL and WDM6 microphysics schemes used in this study predict number concentration of cloud condensation nuclei (CCN). Finally, the NSSL scheme predicts graupel bulk volume in addition to mass mixing ratio and total number concentration, from which the bulk density can be readily diagnosed. Thus,

bulk graupel density in this scheme is not a constant as in the other schemes. Further, newer versions of the NSSL scheme (not examined here) additionally predict the bulk volume of hail. For a short summary of the microphysics schemes evaluated, we refer the reader to the appendix of M15. We point out that improvements and tuning are frequently made to microphysics schemes and, therefore, the same schemes in different versions of WRF may produce differing results.

To create realistic polarimetric radar signatures, minor modifications are made to the MY2 scheme. The default MY2 scheme in WRF v3.5.1 contains a parameter named “Dh_min” for the mean mass diameter of hail set to 5 mm, which converts hail smaller than this threshold to graupel. This almost completely shuts down hail production in our supercell simulation, consistent with the results of Van Weverberg et al. (2012). Thus, for the MY2 experiment, Dh_min is set to 0 mm so that an adequate amount of hail can be produced within the simulated supercell storm and to be more consistent with MY05a and MY05b, which did not contain this parameter.

c. Polarimetric radar data simulator

The polarimetric radar simulator described in J10a and the melting treatment described in D14 are used in this study in order to calculate polarimetric variables from WRF Model output (i.e., predicted mass, and number concentration when applicable). The microphysics schemes used do not explicitly predict the water fraction of frozen particles, which is needed to properly compute their scattering amplitudes. In the schemes, meltwater is removed from frozen particles during the forward integration and added to rainwater, leaving all frozen particles dry. Therefore, we emphasize that “melting” or “wet” frozen particles are *diagnosed* by the polarimetric radar simulator, and *not* simulated within the microphysics schemes themselves.

For most of the microphysics schemes evaluated, the PSD for each hydrometeor species is generally described by an exponential distribution, which is a special case of the gamma PSD given in Eq. (1) with the shape parameter α set to 0. There are a few exceptions to this. Snow in the Thompson scheme follows a PSD that is a linear combination of exponential and gamma distributions (Field et al. 2005; Thompson et al. 2008). Rain and snow hydrometeors in the NSSL scheme assume a mass-dependent gamma distribution (although in newer releases of the WRF Model, rain follows a diameter-dependent distribution), and hail follows a gamma distribution with $\alpha = 1$ [for more details, the reader is referred to Mansell et al. (2010)]. Finally, rain in the WDM6 scheme follows a gamma distribution with $\alpha = 1$. Cloud droplets and cloud ice are currently not

used in the simulator, although the inclusion of cloud ice is planned in the near future.

Each PSD is discretized in order to employ the **T**-matrix method (Waterman 1969; Vivekanandan et al. 1991) to calculate forward- and backward-scattering amplitudes of the rain, snow, graupel, and hail particles, so that Mie scattering effects can be accounted for in the simulation. To improve efficiency, the scattering amplitudes are pre-calculated and stored in lookup tables. We note here that the differing graupel bulk density assumptions in the evaluated microphysics schemes are generally not included in the simulator, as the scattering lookup tables for dry graupel are computed with a constant density of 500 kg m^{-3} . This should not be a substantial source of error, as the microphysics schemes evaluated that do not predict graupel density assume a graupel bulk density of either 400 or 500 kg m^{-3} , which does not differ much (if at all) from the 500 kg m^{-3} assumed by the simulator. In the case of the NSSL scheme, both the mean and median of the predicted graupel density of dry rimed particles at $t = 100 \text{ min}$ vary between 400 and 500 kg m^{-3} which is close to the assumed graupel density for the lookup tables. For all wet frozen hydrometeors, the increased density associated with adding water via the diagnostic water fraction method is automatically taken into account since the scattering lookup tables of wet frozen hydrometeors vary with water fraction. Scattering lookup tables that vary with dry rimed-ice density are planned for the future. We also note here that the unique snow parameterizations (i.e., nonspherical snow, varying density) in the MY2 and Thompson schemes are currently not included in the simulator. This may not be a major issue for supercell simulations as the contribution of snow to polarimetric signatures is much smaller than those from rain and/or rimed ice. This should be improved when the simulator is applied to winter precipitation systems. From the calculated scattering amplitudes, Z_{DR} and K_{DP} are calculated following Zhang et al. (2001) and the formulation for cross-correlation coefficient ρ_{HV} can be found in J10a. The simulator assumed the S-band wavelength in all calculations in this study.

At a given grid point, the mass of water available to attempt to saturate wet and melting snow, graupel, and hail is determined by the total rainwater mass. The percentage of rainwater available to each species is equal to the percentage of the individual frozen species' mass among the total mass of snow, graupel, and hail. The water fraction of snow is calculated as in Jung et al. (2008, hereafter J08). Graupel and hail water fraction is calculated using the iterative method of D14. This modification allows water fraction to vary across the rimed-ice distributions, rather than using the single value water fraction across the distributions as in J08. This captures rimed-ice characteristics (such as spherical hail tumbling

or oblate hail with a water shell) as a function of diameter, not just one characteristic for all particles. The water fraction treatment deviates slightly from D14 in that some of the available rainwater is first “soaked” into the graupel and hail distributions until the bulk density increases to 910 kg m^{-3} , then the soaked rainwater is assumed to be frozen. Next, the total critical water mass of the graupel/hail distributions, denoted as $q_{\text{crit},g/h}$, is calculated by summing the maximum water mass allowed on the surface (i.e., the water “shell”) of the graupel/hail over each diameter bin. For graupel/hail with diameter of 8 mm or less, the graupel/hail is assumed to be completely melted and water fraction is set to 1. Rain mass present in these rimed-ice diameter bins is returned to the rain field. For graupel/hail with diameter greater than 8 mm , the critical water mass that melting graupel/hail can hold on its shell prior to shedding is defined in Rasmussen and Heymsfield (1987). If $q_{\text{crit},g/h}$ is larger than the mass of rain available, $q_{\text{crit},g/h}$ is set to the mass of rain available. Otherwise, $q_{\text{crit},g/h}$ is added to $q_{g/h}$, the PSD is modified based on the new value of $q_{g/h}$, and iteration continues until $q_{\text{crit},g/h}$ converges to a value. For those schemes that have 2M graupel and hail, N_t is adjusted such that the mean mass diameter (D_m) is maintained. Mean mass diameter D_m of spherical hydrometeors is given by

$$D_m = \left(\frac{6\rho_a q}{\pi\rho N_t} \right)^{1/3}, \quad (3)$$

where ρ_a is the ambient air density and ρ is the bulk density of the hydrometeor. For those schemes with 1M graupel, the corresponding fixed or diagnostic N_0 is used to update N_t . Additional details on the iterative procedure can be found in D14.

It should be noted that simulated polarimetric variables are sensitive to the shape and orientation of particles that have to be specified in the simulator. As these parameters can vary quite a lot spatially and temporally among precipitation systems (e.g., Straka et al. 2000), the analyzed polarimetric signatures are not necessarily absolute, but still yield valid comparisons between the schemes. We use the following settings from J08: rain axis ratio follows Brandes et al. (2002), and dry rimed-ice axis ratio is set to 0.75 drawn from the results of Knight (1986). Further, wet rimed-ice axis ratio is simulated as in D14 following Rasmussen and Heymsfield (1987). Rain mean canting angle and standard deviation of canting angle are set to 0° (Hendry and McCormick 1976), and snow mean canting angle and standard deviation of canting angle are set to 0° and 20° , respectively. Rimed-ice mean canting angle is also set to 0° and the standard deviation of canting angle varies with water fraction with a maximum of 60° assumed for

dry rimed-ice as described in J08. This varying standard deviation of rimed-ice canting angle is meant to account for tumbling of dry hail (high standard deviation of canting angle), while wet hail (low standard deviation of canting angle) can be simulated as more stable. For more details, the reader is referred to J08.

3. Simulated polarimetric signatures

As observed polarimetric signatures are related to the microphysics and dynamics of the supercell storm, they are mostly present and persistent throughout the duration of a mature supercell (e.g., Hubbert et al. 1998; KR08; Romine et al. 2008). In our simulations, the supercell becomes mature and the maximum updraft speed becomes quasi-steady by $t = 60$ min. With this in mind, we choose to analyze polarimetric signatures at $t = 100$ min, except for the WDM6 simulation. In that case we examine the signatures at $t = 120$ min, since the supercell storm in the WDM6 simulation takes longer to mature. After sampling polarimetric signatures at a few model times after 100 min, we are confident that the simulations generally produce simulated polarimetric signatures (when present) as persistent as the corresponding observed ones (not shown). Further, we focus our discussion of polarimetric signatures present in the right-moving cell, which is favored in a veering environmental wind shear (e.g., Klemp and Wilhelmson 1978; Rotunno and Klemp 1982; Klemp 1987).

First, we compare the simulated reflectivity at horizontal polarization, Z_H , at the first model level above ground (approximately 0.25 km) for various microphysics schemes (Fig. 1). Compared to other storms, the storm produced with the WDM6 scheme has weaker reflectivity and a smaller forward-flank (FF) in general (Fig. 1e). This behavior is consistent with the results from the real-time storm-scale ensemble forecasts produced by the Center for the Analysis and Prediction of Storms (CAPS) for the 2013 NOAA Hazardous Weather Testbed (HWT) Spring Experiments (SEs) (e.g., Kong et al. 2007; Xue et al. 2007, 2008, 2010a; Kong et al. 2014) where the WDM6 scheme produced a persistently smaller stratiform rain area than other schemes. The overall structure is more similar to the supercell storm simulated with a 1M scheme in J10a. We speculate that this is partly because frozen species are 1M in the WDM6 scheme and the source of rain in stratiform rain is primarily from melting frozen particles (snow and graupel/hail). The low values of reflectivity could partly be due to no graupel reaching the lowest model level (Fig. 2m), as other scheme's reflectivity cores near the surface are

generally collocated with nonzero rimed-ice mass (Figs. 2 and 3).

For the remaining schemes, the MY2 and NSSL schemes produce the largest maximum values of Z_H , reaching 70–75 dBZ (Figs. 1b,c). This is due to the presence of large hail in the area (Fig. 3). While the nonzero values of hail water fraction f_{wh} (Figs. 3c,f) indicate that the hail is wet, reflectivity appears to be more sensitive to hail size in these schemes. The Thompson scheme also produces large maximum values of Z_H (Fig. 1d). Large amounts of medium-sized wet graupel (Figs. 2j–l) reaches the lowest model level, with the largest graupel found in the area with the largest Z_H . Medium-sized graupel with high water fraction (Figs. 2b,c) reaches the lowest model level in the Morrison scheme, but Z_H in this area (Fig. 1a) is relatively low compared to the other microphysics schemes' reflectivity cores collocated with rimed ice. This is due to the small amount of graupel reaching the lowest model level in the Morrison scheme, as q_g is less than 0.25 g kg^{-1} (Fig. 2a).

North–south vertical cross sections of reflectivity are taken through the region of maximum vertical velocity (i.e., updraft of the right-moving cell, Fig. 4) in each experiment. Locations of the vertical cross sections are indicated by the black lines in Fig. 1. The 0°C isotherm is shown to indicate the approximate melting level. Reflectivity cores in the NSSL and Thompson schemes are much more intense than in the other schemes, with Z_H reaching 70–75 dBZ (Figs. 4g,j); this is due to relatively larger graupel in the Thompson scheme (Fig. 5k), and relatively larger hail in the NSSL scheme (Fig. 6c). The WDM6 scheme produces a very sharp gradient of reflectivity below 4 km in the updraft region, dropping from ~ 55 to ~ 30 dBZ (Fig. 4m). This is due to the absence of graupel below 4 km (Fig. 5n) where rain is small (Fig. 5m), although the sudden drop of reflectivity appears to be unphysical. The Morrison, MY2, and WDM6 schemes all produce similar and relatively smaller reflectivity maxima (Figs. 4a,d,m). These maxima are collocated with rimed ice, although the sizes of the rimed-ice particles vary among the microphysics schemes. Small, wet graupel is found in the reflectivity maxima in the Morrison (Figs. 5b,c), MY2 (Figs. 5e,f), and WDM6 (Figs. 5n,o) schemes. Even though hail in the MY2 scheme (Fig. 6a) is larger than graupel in the Morrison and WDM6 schemes, and reflectivity is heavily skewed toward larger hydrometeors (proportional to D^6), the similar reflectivities arise from the fact that the mixing ratio of graupel in the Morrison and WDM6 schemes is much larger than the mixing ratio of hail in the MY2 scheme (not shown). Although rain and graupel sizes in the Morrison (Figs. 5a,b) and WDM6 (Figs. 5m,n)

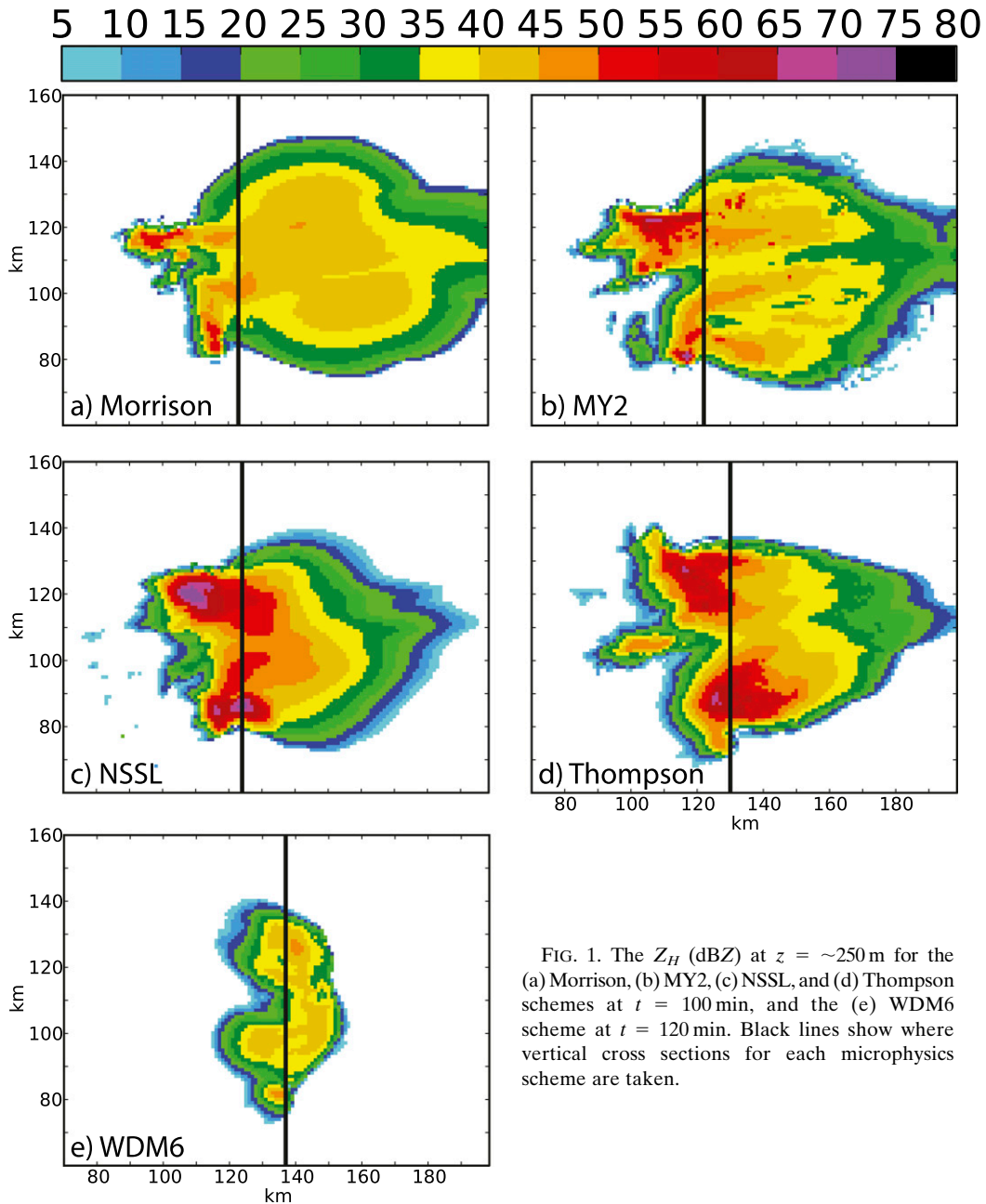


FIG. 1. The Z_H (dBZ) at $z \approx 250$ m for the (a) Morrison, (b) MY2, (c) NSSL, and (d) Thompson schemes at $t = 100$ min, and the (e) WDM6 scheme at $t = 120$ min. Black lines show where vertical cross sections for each microphysics scheme are taken.

schemes are similar in the reflectivity maxima, graupel still contributes to the reflectivity maxima slightly more than rain in these schemes (not shown). Thus, the magnitude of the reflectivity core in each microphysics scheme tends to be dominated by the size and amount of rimed ice.

a. Z_{DR} and K_{DP} columns

Large (and therefore oblate) raindrops and oblate wet rimed ice that can be advected above the melting layer by the convective updraft contribute to large Z_{DR} values

in the Z_{DR} column (Illingworth et al. 1987; Conway and Zrnić 1993; Brandes et al. 1995; Loney et al. 2002). High liquid water mass from raindrops shed from either falling melting hail or hail experiencing wet growth, or water mass on the mixed-phased particles themselves, form a region of high K_{DP} located near the updraft referred to as the K_{DP} column (Hubbert et al. 1998; Loney et al. 2002).

All of the microphysics schemes examined produce Z_{DR} and K_{DP} columns that penetrate the melting level (marked by the 0°C isotherm in the reflectivity plots in

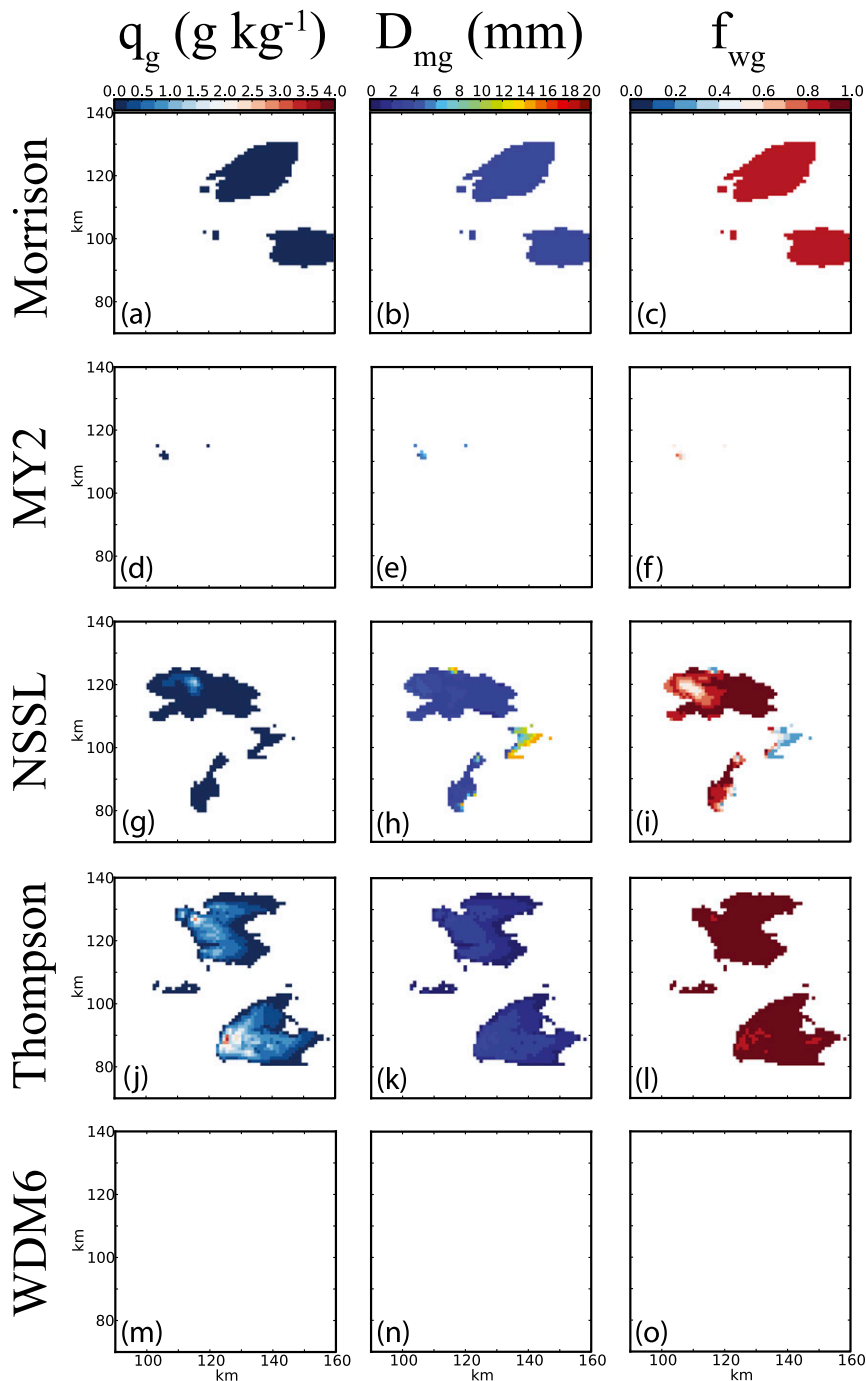


FIG. 2. The q_g (g kg^{-1}), D_{mg} (mm), and f_{wg} at $z \approx 250$ m for the (a)–(c) Morrison, (d)–(f) MY2, (g)–(i) NSSL, and (j)–(l) Thompson schemes at $t = 100$ min, and the (m)–(o) WDM6 scheme at $t = 120$ min.

Fig. 4), though their magnitudes and depths vary considerably (Fig. 4). Locations of the vertical cross sections are indicated by the black lines in Fig. 1. Vertical velocity contours are included on the Z_{DR} and K_{DP} plots to highlight the updraft regions. The Z_{DR} contours are overlaid on the hydrometeor mean mass diameter and

water fraction plots in Figs. 5 and 6 to highlight the Z_{DR} columns.

The overall Z_{DR} values in the column are the lowest in the NSSL scheme, with Z_{DR} of 0.5–2.0 dB (Fig. 4h), and highest in the Thompson scheme, with Z_{DR} of 3.5–4.5 dB (Fig. 4k). This can be explained by examining D_{mr} , $D_{mg,h}$,

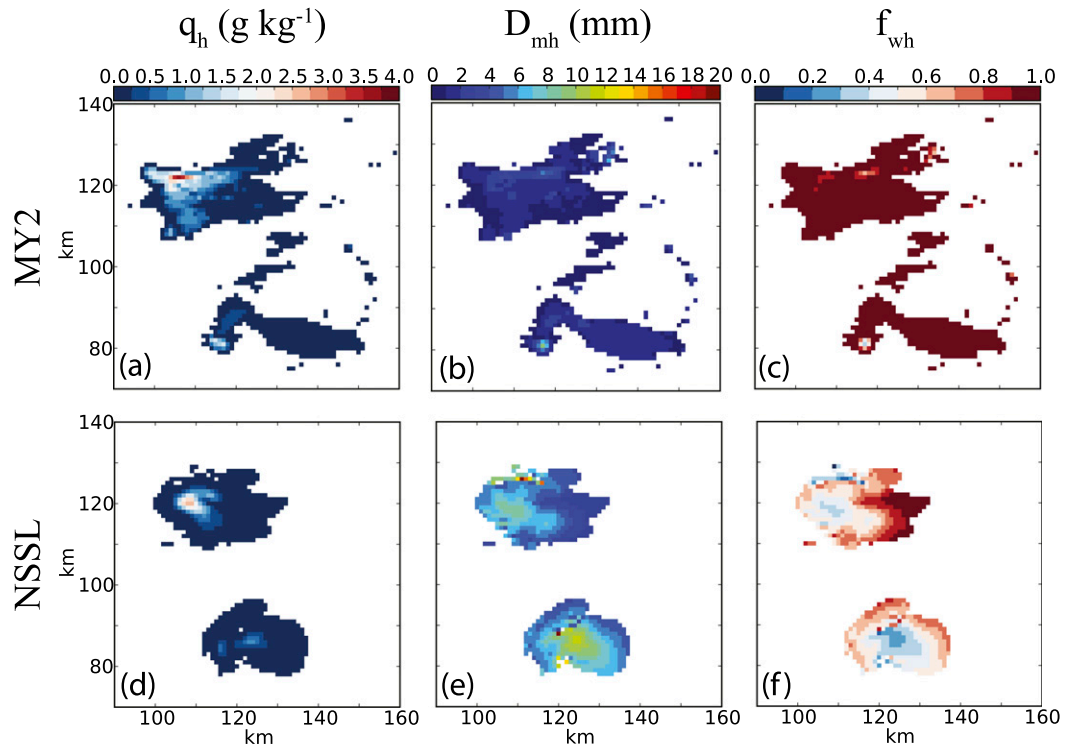


FIG. 3. The q_h (g kg^{-1}), D_{mh} (mm), and f_{wh} at $z \approx 250$ m for the (a)–(c) MY2 and (d)–(f) NSSL schemes at $t = 100$ min.

and rimed-ice water fraction ($f_{wg,h}$) (Figs. 5 and 6). The relatively low Z_{DR} values of the NSSL scheme in the column are due to the presence of dry, large hail with D_{mh} greater than 1 cm (Figs. 6c,d). Large and rather dry hailstones reduce Z_{DR} because these particles can gyrate and tumble (e.g., Knight and Knight 1970; Thwaites et al. 1977; Rasmussen and Heymsfield 1987), which would cause them to appear more spherical in shape on average to radars. This large, dry hail overshadows the raindrops' contribution to Z_{DR} , given that the NSSL scheme actually produces relatively larger raindrops with D_{mr} exceeding 1 mm occasionally in the column (Fig. 5g). Raindrops become increasingly oblate as diameter increases, which increases Z_{DR} . The Z_{DR} from wet graupel is significantly influencing the column more than rain in the Thompson scheme (not shown), as graupel in the column is relatively large with D_{mg} of 2–6 mm (Fig. 5k) and with high water fraction f_{wg} (Fig. 5l). However, the majority of raindrops are small with D_{mr} less than 0.75 mm (Fig. 5j). Medium-sized ($< \sim 1$ cm) wet hail and graupel produce large Z_{DR} values because of the liquid torus around the rimed-ice equator which aerodynamically stabilizes the particle (Rasmussen et al. 1984; Rasmussen and Heymsfield 1987) and thus maintains an oblate shape. On the other hand, raindrops become increasingly spherical with decreasing diameter,

reducing Z_{DR} . In all cases, the Z_{DR} column is dominated by the contribution from fully or partially melted rimed ice as diagnosed by the simulator (not shown).

The Thompson scheme produces unrealistically large K_{DP} values of $8^\circ\text{--}10^\circ \text{ km}^{-1}$ (Fig. 4l) in the K_{DP} column. While much larger K_{DP} values are sometimes observed for water-coated hail, typical values of K_{DP} range from 0° to 3° km^{-1} at the S band (e.g., Straka et al. 2000; Schuur et al. 2003; Ryzhkov et al. 2005). The K_{DP} columns are generally collocated with and sensitive to regions of relatively higher q_r (Fig. 7). Typically, liquid water mass on frozen hydrometeors are kept in their respective frozen hydrometeor mass fields as in Figs. 2 and 3, with the transferred water mass subtracted from the q_r field in order to treat q_r as pure rain. Since K_{DP} is strongly dependent on liquid water mass, however, we include all liquid water mass (even on frozen hydrometeors) in the q_r field in Fig. 7 for ease of comparison. The sensitivity of K_{DP} to liquid water mass on wet rimed ice is specifically evident in the WDM6 scheme, where K_{DP} values drop substantially from $4^\circ\text{--}5^\circ \text{ km}^{-1}$ to $0^\circ\text{--}0.25^\circ \text{ km}^{-1}$ (Fig. 4o) at model levels below the presence of wet graupel (Figs. 5n,o). This K_{DP} decrease can also be partially attributed to the presence of small raindrops (Fig. 5m), as K_{DP} is also related to the axis ratio of hydrometeors. While the Thompson scheme produces high

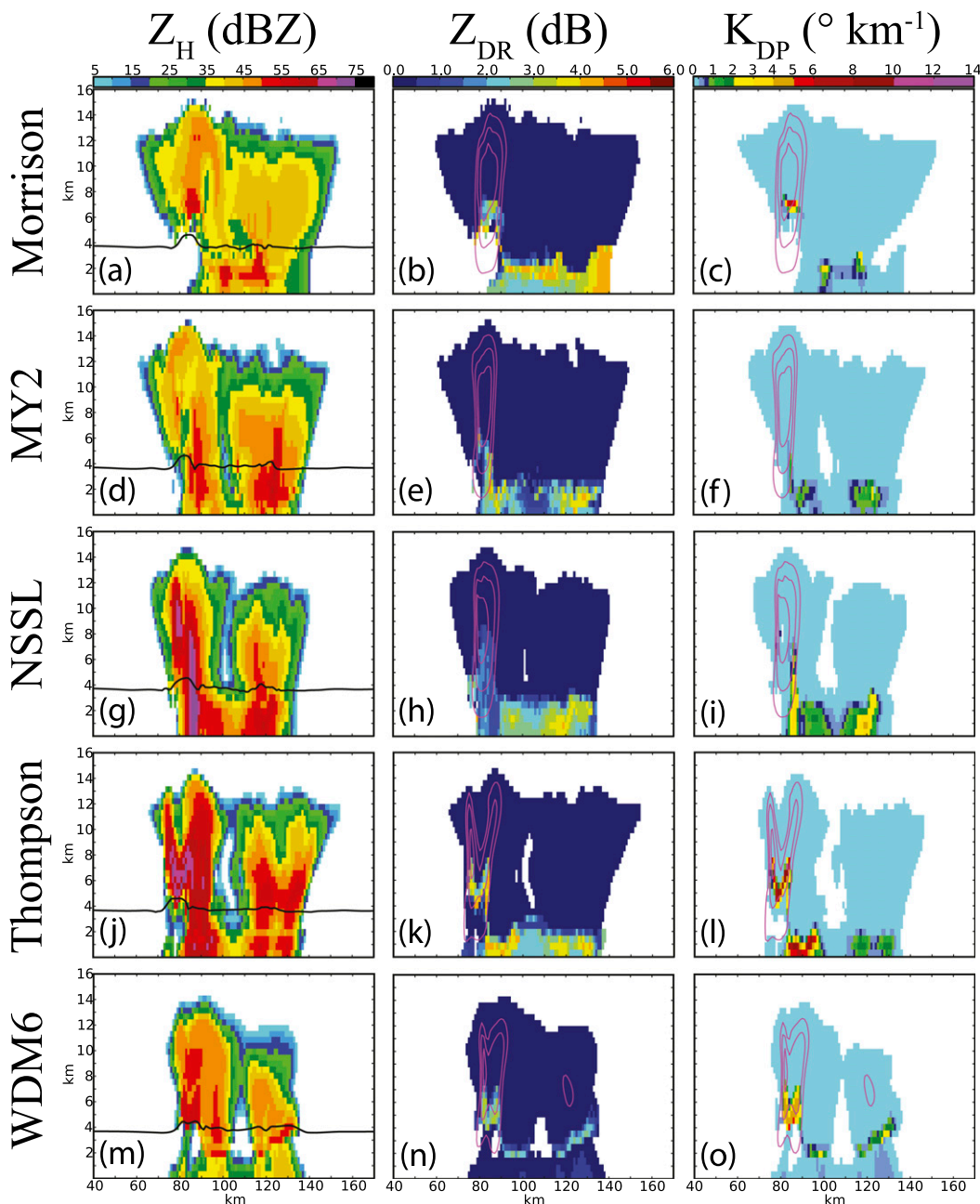


FIG. 4. The Z_H (dBZ), Z_{DR} (dB), and K_{DP} ($^{\circ} \text{km}^{-1}$) columns for the (a)–(c) Morrison, (d)–(f) MY2, (g)–(i) NSSL, and (j)–(l) Thompson schemes at $t = 100$ min, and the (m)–(o) WDM6 scheme at $t = 120$ min. Vertical velocity contours are shown in Z_{DR} and K_{DP} plots with contours of 15 m s^{-1} starting from 10 m s^{-1} . The 0°C isotherm is shown in Z_H plots.

values of q_r that are greater than 6 g kg^{-1} in the K_{DP} column (Fig. 7d), D_{mr} is less than 0.75 mm (Fig. 5j). Since wet graupel with D_{mg} ranging from 6 to 7 mm (Figs. 5k,l) is present for the largest K_{DP} values, the liquid water mass residing on wet graupel is responsible for the large K_{DP} values in the scheme. The MY2 scheme produces the lowest K_{DP} values in the column among the

microphysics schemes, ranging from 0° to $1.5^{\circ} \text{ km}^{-1}$ (Fig. 4f). This is a result of low q_r produced by the scheme (Fig. 7b).

Aside from the columns in the main updraft of the right mover, the WDM6 scheme exhibits a region of increased Z_{DR} and K_{DP} primarily below the melting layer in the left-moving cell, as shown in Figs. 4n and 4o.

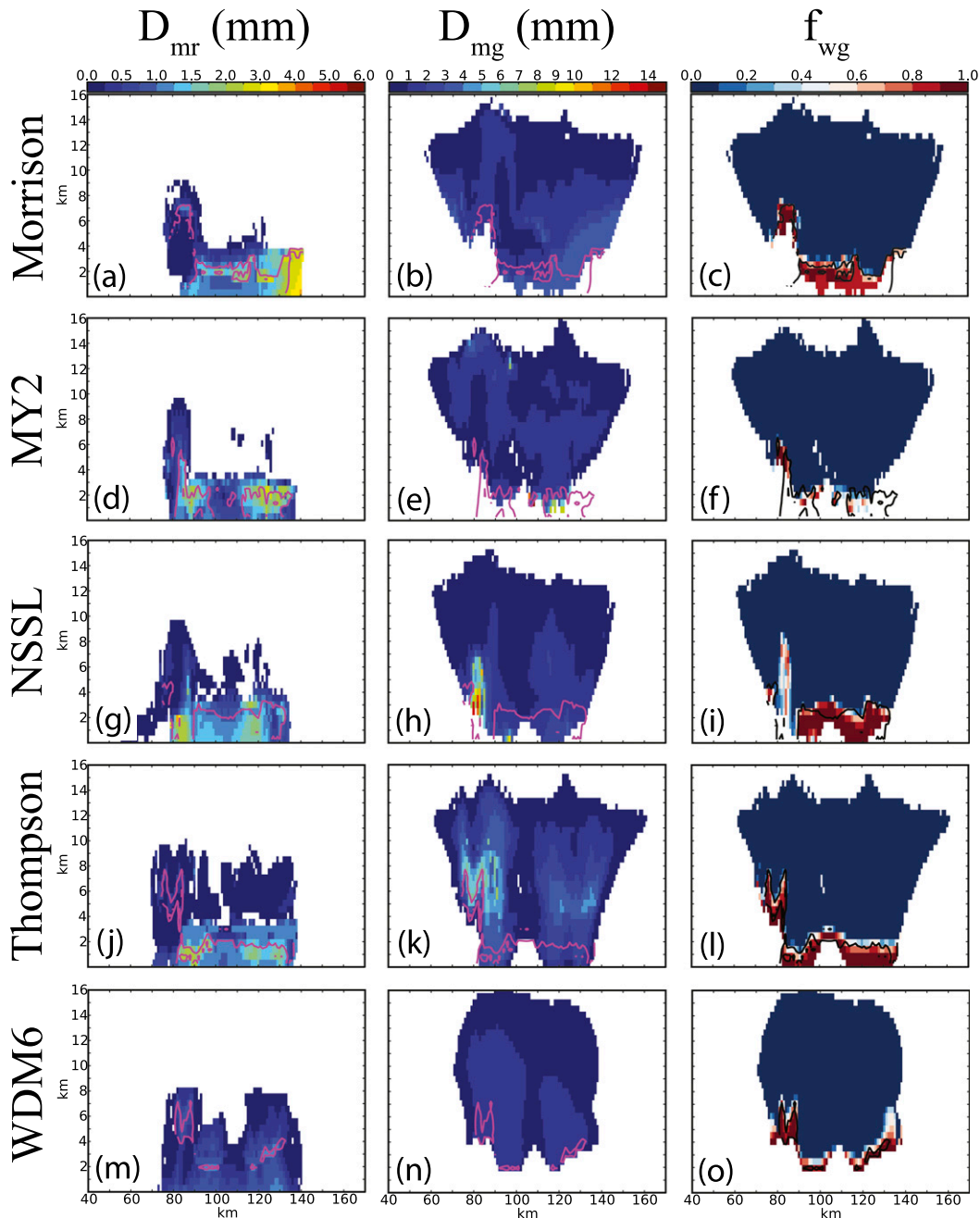


FIG. 5. The D_{mr} (mm), D_{mg} (mm), and f_{wg} as in Fig. 4. The Z_{DR} (dB; magenta in D_m plots, black in f_{wg} plots) contours are shown for the 2- and 4-dB levels.

This increased Z_{DR} and K_{DP} is from somewhat oblate rain (Figs. 5m and 7e) and wet graupel (Figs. 5n,o) near the updraft of the left-moving cell that is within this vertical cross section, and this appears to be physical. Another remarkable difference of the WDM6 scheme is the extremely low Z_{DR} and K_{DP} values near the surface (Figs. 4n,o) compared to the other schemes. This can be directly attributed to the relatively smaller max D_{mr} in

the WDM6 scheme compared to the other schemes (Fig. 5m), and the lack of wet graupel reaching the lowest model level (Figs. 5n,o).

b. Z_{DR} arc

The Z_{DR} arc in a supercell storm is formed by the size sorting of hydrometeors by storm-relative winds (Ryzhkov et al. 2005; KR08; KR09; Kumjian and

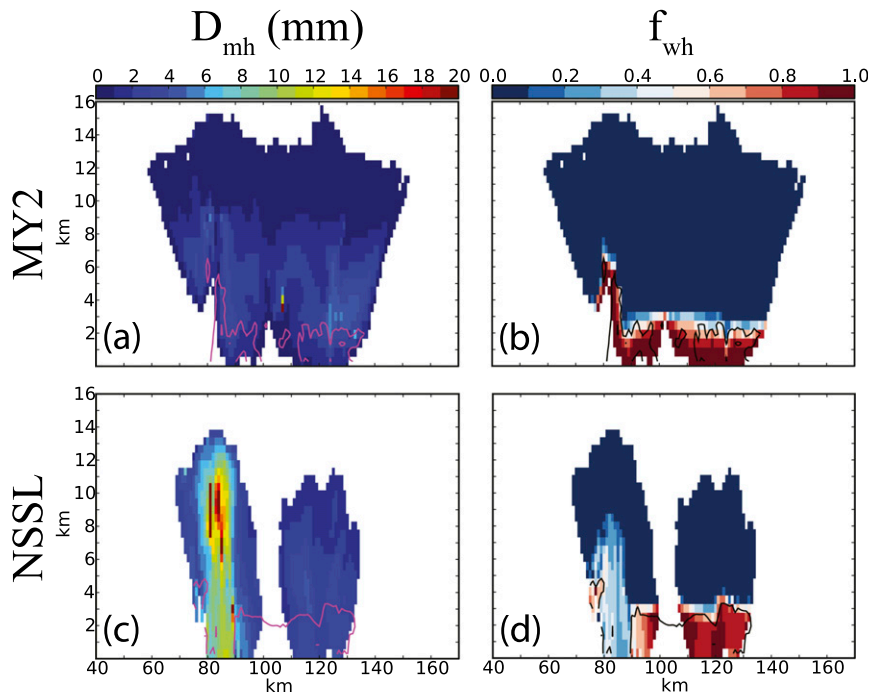


FIG. 6. The D_{mh} (mm) and f_{wh} for the (a),(b) MY2 and (c),(d) NSSL schemes at $t = 100$ min. The Z_{DR} (dB; magenta in D_{mh} plots, black in f_{wh} plots) contours are shown for the 2- and 4-dB levels.

Ryzhkov 2012; Dawson et al. 2015a). Storm-relative winds advect hydrometeors as they fall through a given layer of the atmosphere, and a Z_{DR} gradient forms in the direction of the storm-relative mean wind (Dawson et al. 2015a) due to differing terminal velocities of smaller (spherical) and larger (more oblate) hydrometeors. Focusing on the right mover in this section, the Z_{DR} arc is adjacent to the southern edge (Ryzhkov et al. 2005; KR08; KR09).

The simulated Z_{DR} arc seems to be primarily influenced by the size sorting of graupel and hail, rather than the size sorting of rain (D14). Consistent with the findings of D14, the Thompson and WDM6 schemes fail to produce a Z_{DR} arc, perhaps because they are 1M for the graupel species (Figs. 8g,i). On the other hand, the schemes that contain 2M rimed-ice categories (Morrison, MY2, and NSSL) are able to produce a Z_{DR} arc (Figs. 8a,c,e). The Z_{DR} arcs in the Morrison scheme are symmetric and have the highest Z_{DR} values, reaching 4.5 dB (Fig. 8a). In this area, D_{mr} is much larger (Fig. 8b) than in the Z_{DR} arcs of the MY2 and NSSL schemes. Qualitatively speaking, the NSSL scheme produces the location and structure of the Z_{DR} arc that compares most favorably with observations (e.g., KR08). The Z_{DR} arc in the NSSL scheme is located on the edge of the right-moving supercell (Fig. 8e), while the Z_{DR} arc in the MY2 scheme is slightly farther into the forward flank

(Fig. 8c). The Z_{DR} arc in the MY2 scheme is slightly stronger in magnitude than the Z_{DR} arc in the NSSL scheme due to wet hail in the MY2 Z_{DR} arc (Figs. 3b,c), although D_{mr} in the MY2 scheme is also slightly larger (Fig. 8).

c. Midlevel Z_{DR} and ρ_{HV} rings

Midlevel Z_{DR} and ρ_{HV} rings exist because frozen hydrometeors melt as they fall around the updraft. Large raindrops and oblate, melting rimed ice around the updraft form a ring-shaped signature of high Z_{DR} , while melting hydrometeors that are large enough to exhibit the resonance effect will substantially decrease ρ_{HV} (KR08). According to KR08, half rings can also appear, and do so on the right flank of the updraft when present.

Since the vertical cross sections of reflectivity indicate the location of the melting level is around 4 km (Fig. 4), horizontal cross sections are taken at approximately 4 km to examine the midlevel Z_{DR} and ρ_{HV} rings (Fig. 9), with vertical velocity contours in the Z_{DR} plots indicating the updraft location. The Z_{DR} contours are overlaid on the mean mass diameter and water fraction plots (Figs. 10 and 11) to observe the hydrometeor characteristics in the Z_{DR} rings. The Morrison, MY2, and Thompson schemes produce the largest Z_{DR} magnitudes of 3.5–4.5 dB (Figs. 9a,c,g), while the WDM6 scheme produces the overall smallest Z_{DR} magnitudes

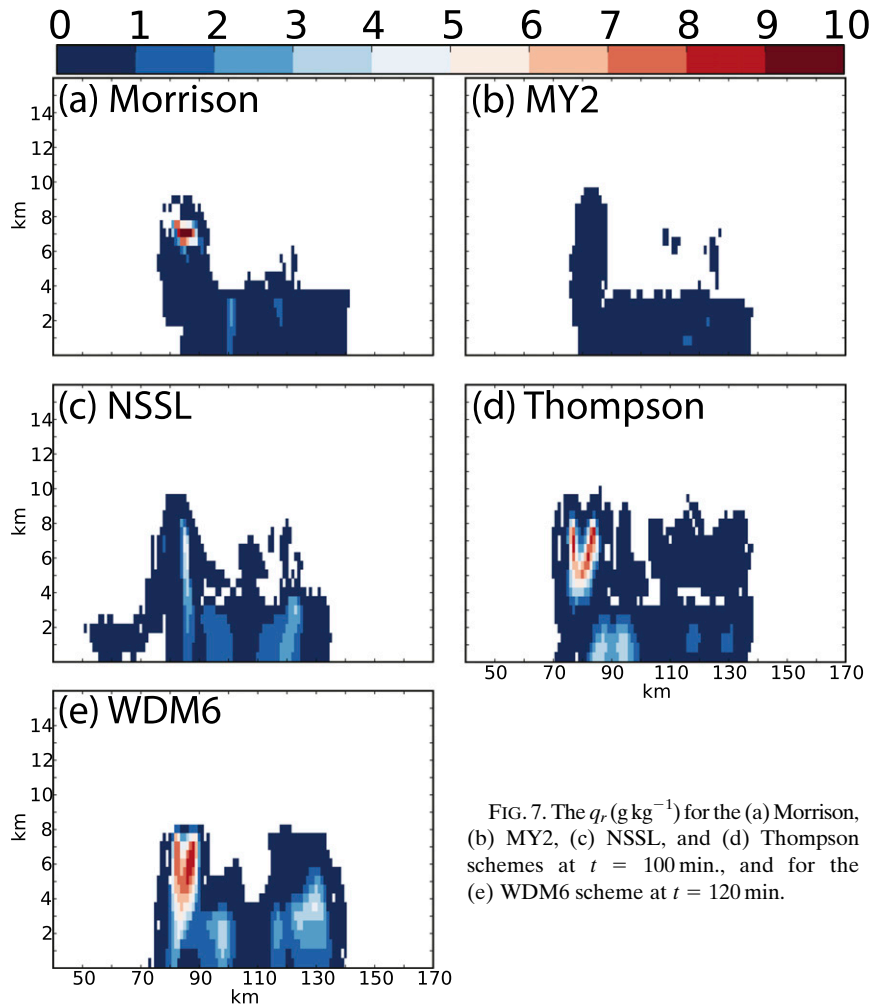


FIG. 7. The q_r (g kg^{-1}) for the (a) Morrison, (b) MY2, (c) NSSL, and (d) Thompson schemes at $t = 100$ min., and for the (e) WDM6 scheme at $t = 120$ min.

of 0.5–3 dB in the simulated ring (Fig. 9i). The high Z_{DR} values in the Thompson scheme appear in a disk shape and do not show a distinct ring or half-ring structure (Fig. 9g), which is similar to those produced by the 1M scheme in J10a. Schemes with the largest Z_{DR} values (Morrison, MY2, Thompson) contain relatively larger raindrops in the overlaid Z_{DR} contours (Figs. 10a,d,j) and medium-sized, wet rimed ice (Figs. 10b,c,k,l and 11a,b) in the vicinity of the ring. While D_{mr} in the WDM6 scheme is not small (Fig. 10m), small wet graupel (Figs. 10n,o) is unable to further increase Z_{DR} . Also of note, the NSSL scheme contains relatively large, oblate raindrops (Fig. 10g) even outside of the Z_{DR} ring. The low Z_{DR} there is due to the compensating presence of large, dry hail (Figs. 11c,d). Generally, a more realistic, almost complete Z_{DR} ring signature is simulated with the MY2 scheme (Fig. 9c). The WDM6 scheme is able to simulate a complete Z_{DR} ring, but with very low Z_{DR} values on the bottom-right flank of the updraft (Fig. 9i). The Morrison and NSSL schemes are also able

to produce a half-ring as has often been observed (e.g., KR08) (Figs. 9a,e).

J10a discussed in depth how hailstones that exhibit the resonance effect can reduce ρ_{HV} (KR08; KR09). The resonance effect occurs in the Mie (or resonance) region where $D|\epsilon|^{1/2}/\lambda$ approaches 1. Here, ϵ is dielectric constant and λ is radar wavelength. In this region, the radar cross section of a particle oscillates as a function of particle size (or radar frequency) instead of increasing with increasing size. In J10a, dry hailstones only marginally decrease ρ_{HV} , and only for very large hailstones. Large wet hailstones reduce ρ_{HV} with significantly smaller diameters than dry hailstones, although the magnitude of the ρ_{HV} reduction decreases with increasing hail water fraction. The largest ρ_{HV} reduction in the midlevel ρ_{HV} rings is found with the NSSL scheme, with ρ_{HV} equal to 0.92–0.94 (Fig. 9f). The presence of relatively large hail that is partially wet (Figs. 11c,d) in the ρ_{HV} reduction suggests that resonance may play a big role. While the Morrison and Thompson schemes

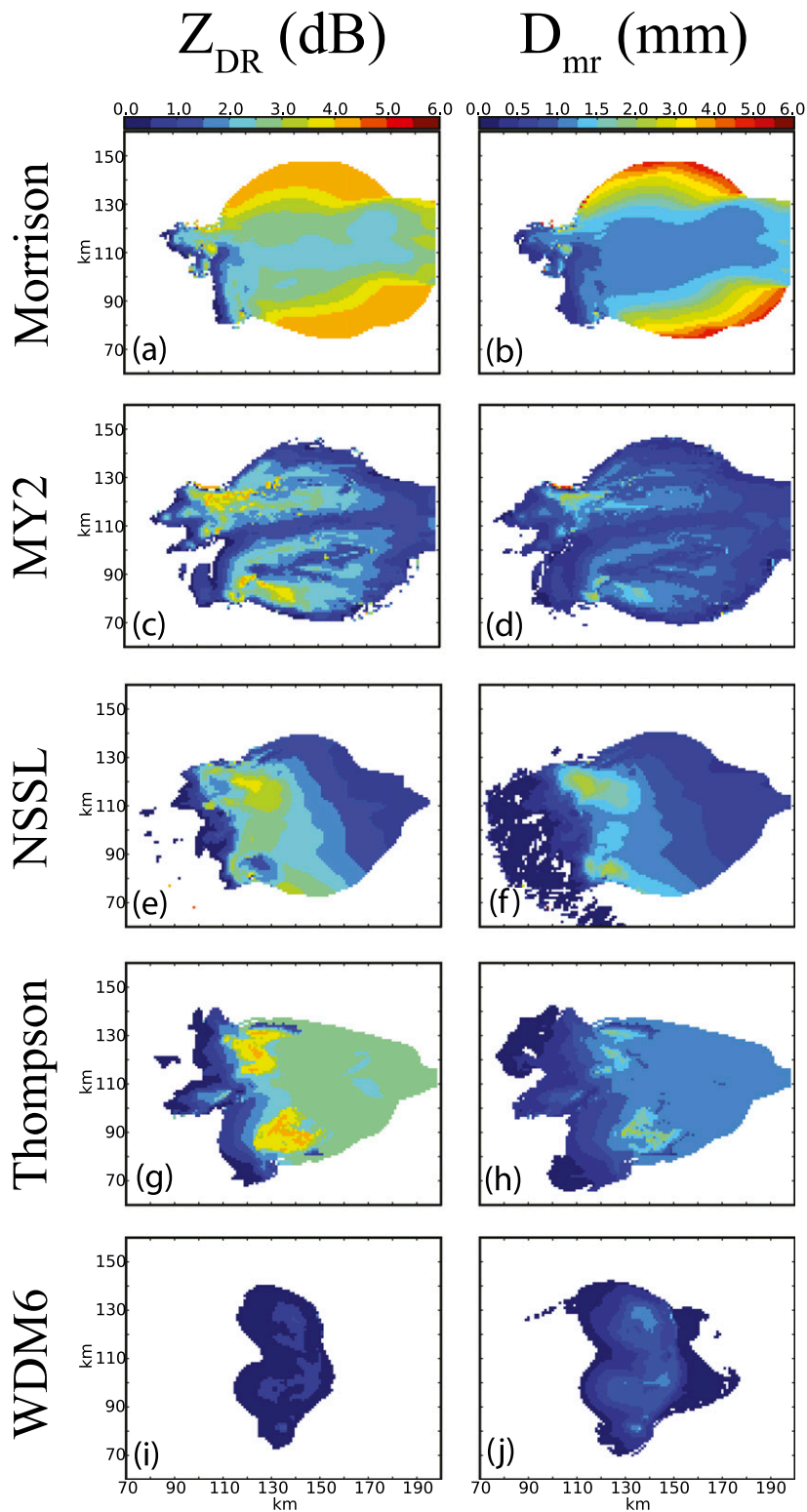


FIG. 8. The Z_{DR} (dB) and D_{mr} (mm) at $z = \sim 250$ m showing Z_{DR} arcs for the (a),(b) Morrison; (c),(d) MY2; (e),(f) NSSL; and (g),(h) Thompson schemes at $t = 100$ min; and the (i),(j) WDM6 scheme at $t = 120$ min.

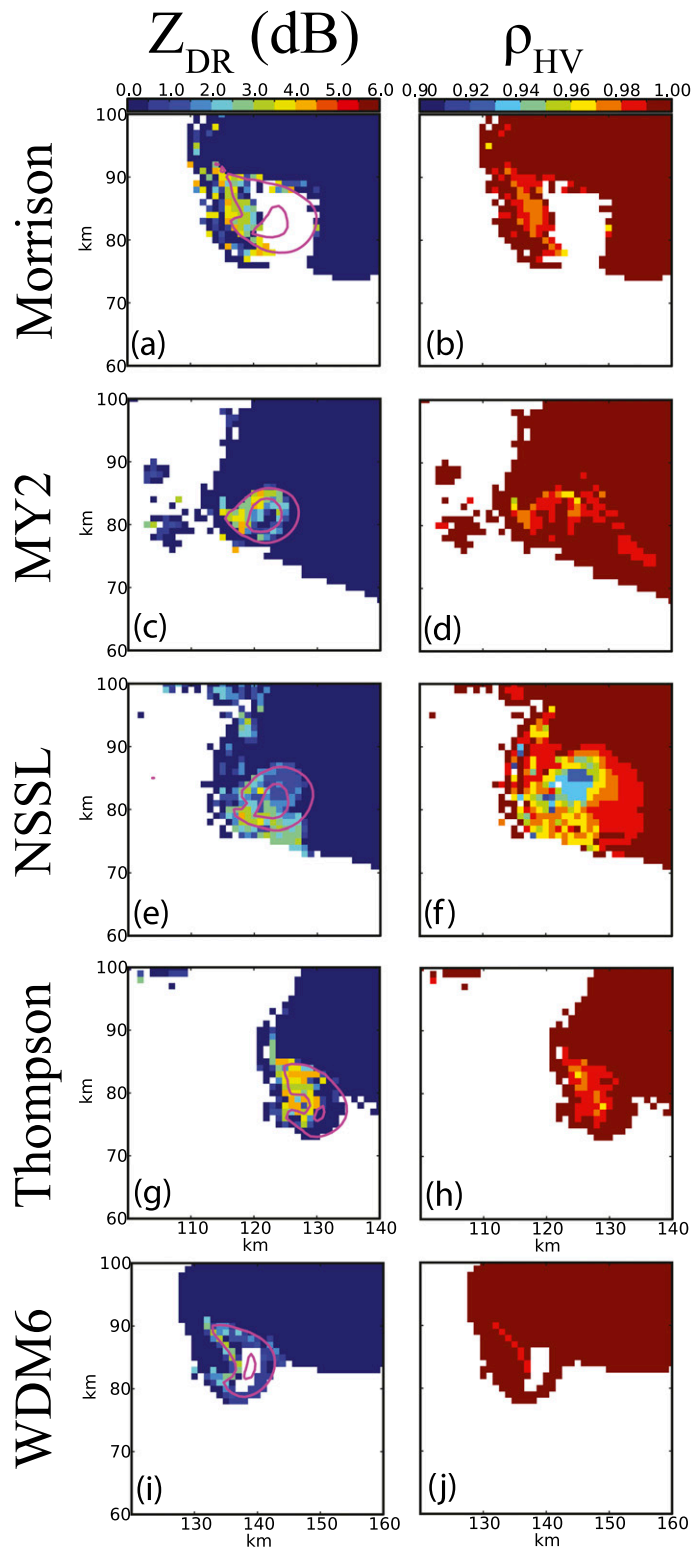


FIG. 9. Midlevel Z_{DR} (dB) and ρ_{HV} at $z \sim 4$ km for the (a),(b) Morrison; (c),(d) MY2; (e),(f) NSSL; and (g),(h) Thompson schemes at $t = 100$ min, and the (i),(j) WDM6 scheme at $t = 120$ min. Vertical velocity contours are shown in Z_{DR} plots with contours of 15 m s^{-1} starting from 10 m s^{-1} .

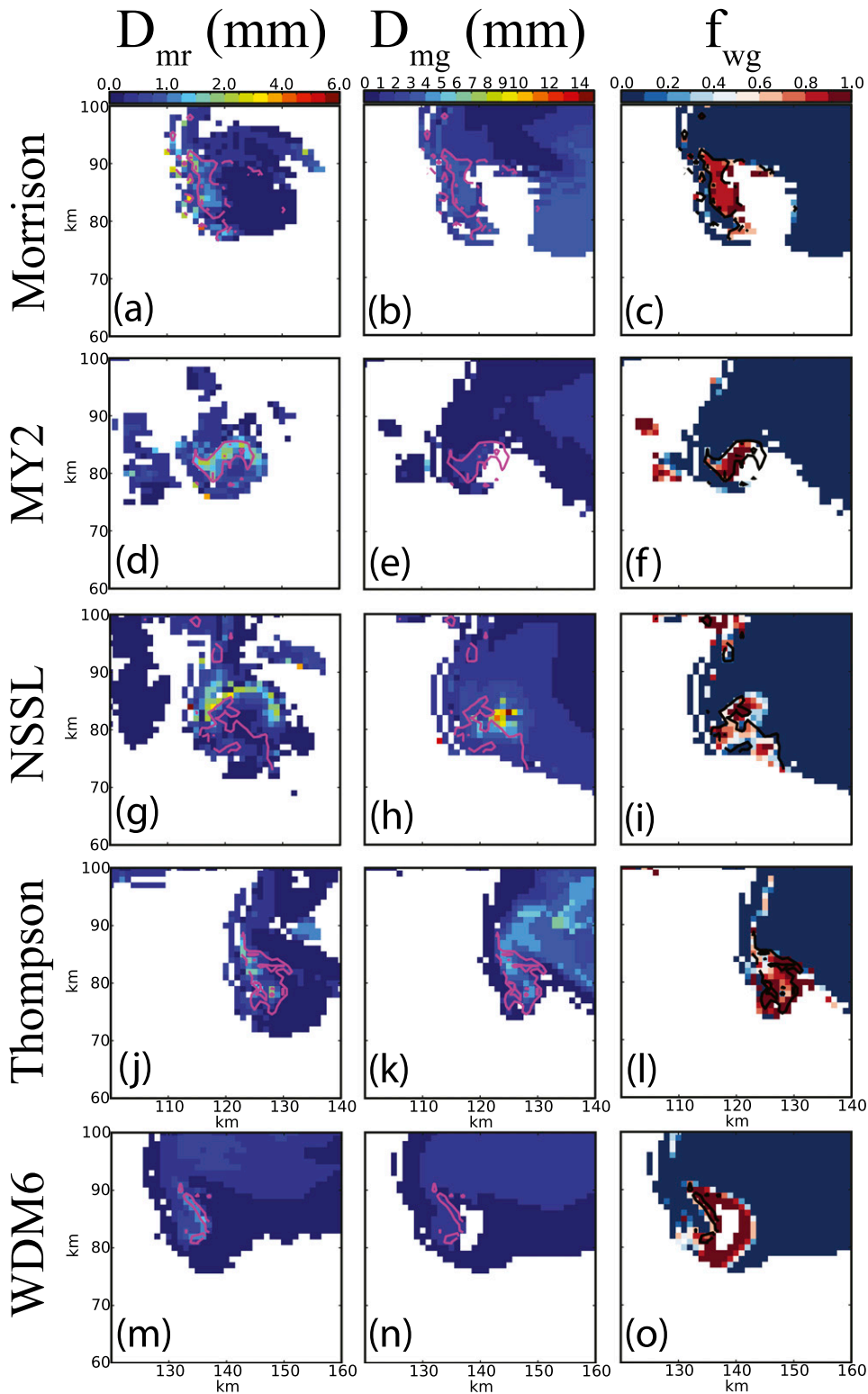


FIG. 10. Midlevel D_{mr} (mm), D_{mg} (mm), and f_{wg} at $z \sim 4$ km for the (a)–(c) Morrison, (d)–(f) MY2, (g)–(i) NSSL, and (j)–(l) Thompson schemes at $t = 100$ min; and the (m)–(o) WDM6 scheme at $t = 120$ min. The Z_{DR} (dB; magenta in D_m plots, black in f_{wg} plots) contours are shown for the 2- and 4-dB levels.

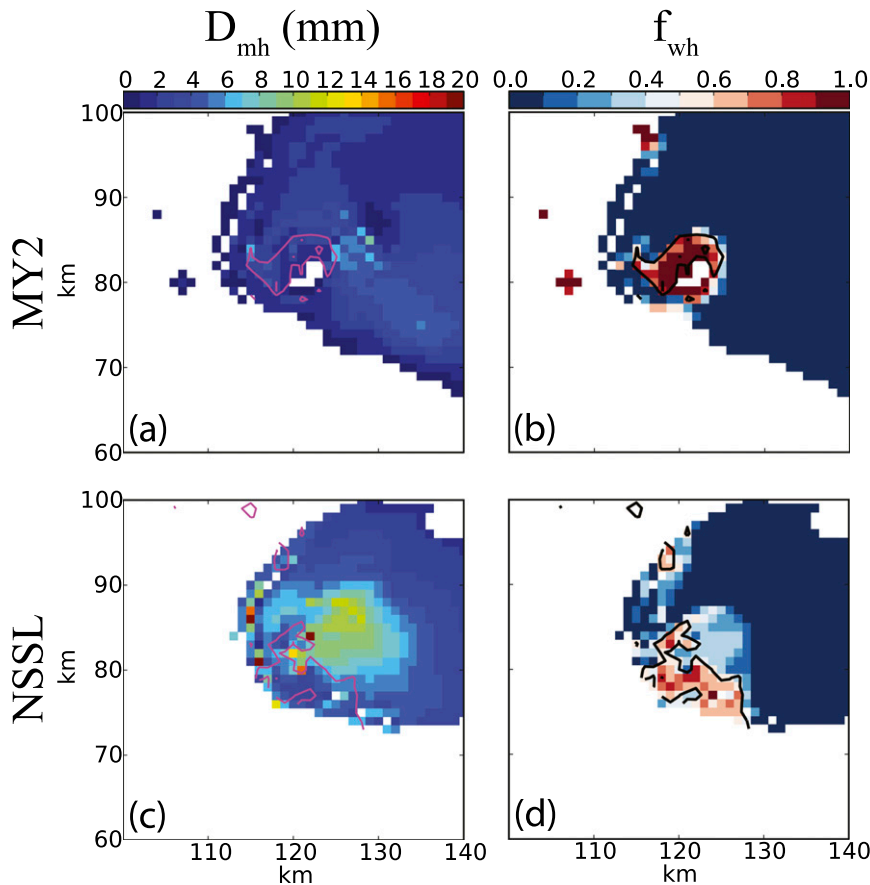


FIG. 11. The D_{mh} (mm) and f_{wh} at $z \sim 4$ km for midlevel rings for the (a),(b) MY2 and (c),(d) NSSL schemes at $t = 100$ min. The Z_{DR} (dB; magenta in D_{mh} plots, black in f_{wh} plots) contours are shown for the 2- and 4-dB levels.

show a region of reduced ρ_{HV} values (Figs. 9b,h) to the left of the updraft, the MY2 and NSSL schemes produce better-defined half-ring and full-ring shapes, respectively (Figs. 9d,f), in the vicinity of the updraft compared to the other schemes. The WDM6 scheme is unable to reproduce a ρ_{HV} ring (Fig. 9j), suggesting that rimed-ice particles (Fig. 10n) produced by the scheme may be smaller than resonance sizes.

d. Hail signature in the forward-flank downdraft

Because large, dry hailstones have the potential to tumble, as they reach the surface an area of low Z_{DR} will form (KR08). The NSSL scheme is the only scheme to produce the hail signature in the forward-flank downdraft, which is centered at $x = 125$ km, $y = 85$ km in Fig. 8e. Large, dry hail (Figs. 3e,f) falls in this area and is associated with a region of reduced Z_{DR} (Fig. 8e). Graupel at the lowest model level in the Morrison and Thompson schemes is medium sized (Figs. 2b,k), but also very wet (Figs. 2c,l), enhancing Z_{DR} . For the WDM6 scheme, no graupel reaches the lowest model level

(Figs. 2n,o). The MY2 scheme has very little graupel near the surface (Figs. 2e,f), although widespread hail is able to reach the lowest model level. This hail is medium sized and mostly melted (Figs. 3b,c), increasing Z_{DR} .

e. K_{DP} foot

The K_{DP} foot is a region of large K_{DP} near the surface that spans from the forward flank into the vicinity of the storm's hook region. High liquid water mass from melting hail is potentially responsible for increased K_{DP} in this signature (Romine et al. 2008). The magnitude of the K_{DP} foot is sensitive to q_r present (which includes liquid water mass on graupel and hail as in section 3a) at the lowest model level (Figs. 12). The Thompson scheme produces the largest K_{DP} values of 10° – 12° km^{-1} (Fig. 12g), while the Morrison, MY2, and WDM6 schemes produce the smallest K_{DP} values in the K_{DP} foot region, which do not exceed 0.75° km^{-1} (Figs. 12a,c,i). As stated in section 3a, typical K_{DP} values range from 0° to 3° km^{-1} . At the lowest model level, the Thompson scheme produces the largest q_r in the K_{DP} foot region

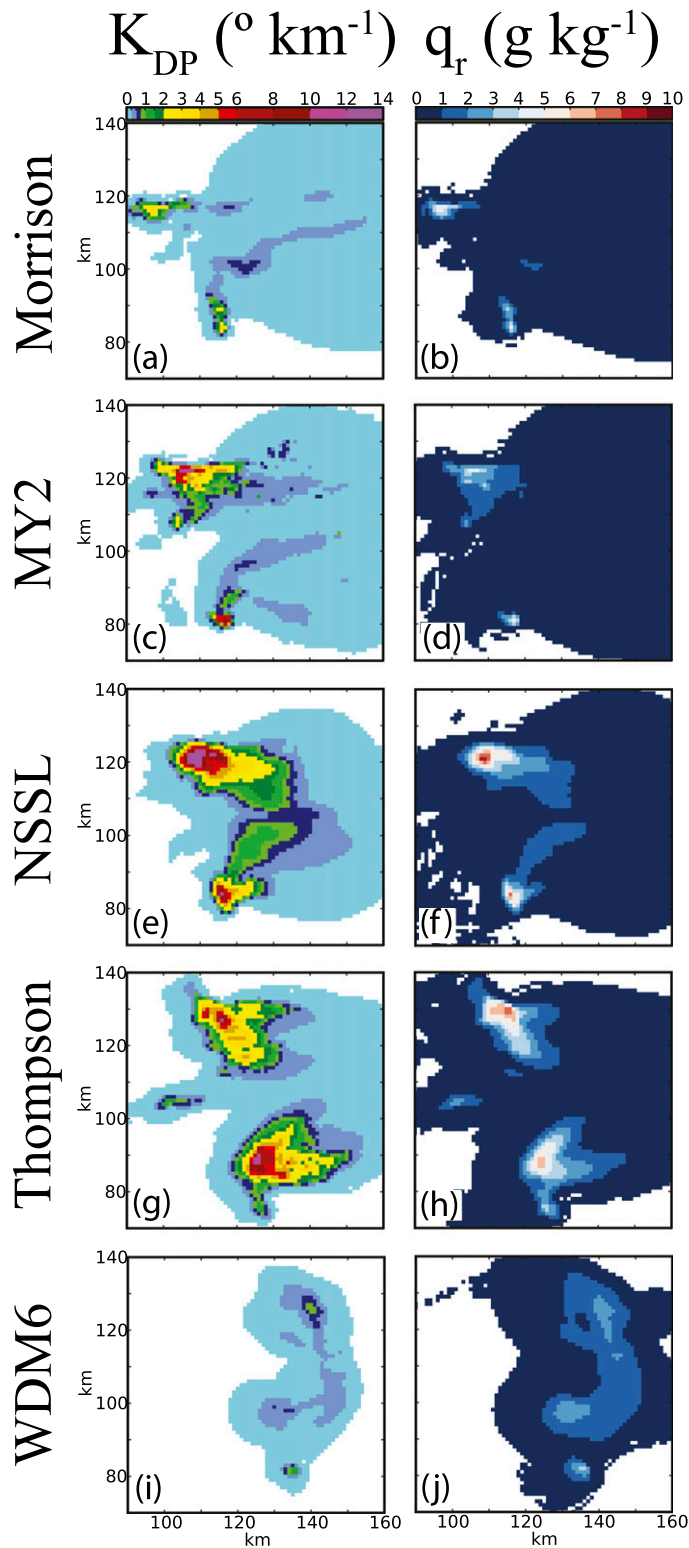


FIG. 12. The K_{DP} ($^{\circ} \text{ km}^{-1}$) and q_r (g kg^{-1}) at $z \approx 250 \text{ m}$ for the (a),(b) Morrison; (c),(d) MY2; (e),(f) NSSL; and (g),(h) Thompson schemes at $t = 100 \text{ min}$, and the (i),(j) WDM6 scheme at $t = 120 \text{ min}$.

(Fig. 12h), while the MY2 scheme produces the lowest q_r (Fig. 12d). Liquid water mass transferred to melting graupel in the Thompson scheme (Figs. 2k,l) in the K_{DP} foot region contributes to the large K_{DP} values. Maximum q_r in the Morrison scheme is comparable to maximum q_r in the NSSL scheme in the K_{DP} foot region (Figs. 12b,f), but larger D_{mr} contributes to higher K_{DP} in the NSSL scheme (Fig. 8). Similarly, the WDM6 scheme produces relatively larger q_r (Fig. 12j) than the Morrison and MY2 schemes in the K_{DP} foot region, but given the relatively small raindrops at the lowest model level (Fig. 8j), K_{DP} is low for this scheme. Outside the hook, enhanced K_{DP} is found in the Morrison and MY2 schemes (Figs. 12a,c) to the left of the updraft. In the Morrison scheme, this is a result of high liquid mass from rain as there is no graupel in this area (Fig. 2a). In the MY2 scheme, this enhanced K_{DP} is primarily from liquid water mass on melting hail (Figs. 3b,c).

4. DSD properties

a. Properties of liquid hydrometeors

Contoured frequency by altitude diagrams (CFADs; Yuter and Houze 1995) (Figs. 13 and 14) are made to gain an understanding of any potential biases in each microphysics scheme. The CFADs show the number of grid-point occurrences, normalized by the total number of grid points that contain a nonzero mass, per 0.25-mm range of D_{mr} and D_{mg} and 0.5-mm range of D_{mh} at each model height level. The plots are normalized in order to provide a basis for comparing the frequency distributions since raw counts are affected by the size of the simulated supercell storm. M15 examined vertical distributions of median volume diameter D_0 of rain relative to a simulated squall line's leading edge for the microphysics schemes that are examined in this study, and found somewhat similar distributions. While median volume diameter is different than the mean mass diameter examined here, parallels can be made nonetheless.

We see that D_{mr} increases with progressively lower model heights near the surface much more for the Morrison and MY2 schemes (Figs. 13a,c) than other schemes. According to M15, these schemes can produce excessive size sorting since the shape parameter α is 0 for the rain PSD. More generally, excessive size sorting of hydrometeors in 2M schemes occurs when even a nonzero fixed α is used (e.g., Wacker and Seifert 2001; MY05a; Milbrandt and McTaggart-Cowan 2010; Kumjian and Ryzhkov 2012). Further, raindrops in the Morrison scheme have the potential to reach the maximum raindrop size threshold in the scheme when the mass of rain is low without much resistance. This is

because raindrop breakup is performed by reducing self-collection, and self-collection is only initiated beyond a mixing ratio threshold. The presence of D_{mr} greater than 1.75 mm with noticeable relative frequency that is found only in the Morrison scheme helps explain why this scheme produces the largest Z_{DR} and D_{mr} in the Z_{DR} arc near the surface (Figs. 8a,b). The remaining schemes do have gradually increasing D_{mr} with progressively lower model heights, and M15 offered the following explanations for the general lack of excessive size sorting present in these schemes. First, the NSSL scheme mitigates excessive size sorting by modifying total number concentration N_t of rain, graupel, and hail during sedimentation to simulate more accurate reflectivity (Mansell 2010). Rain below the melting layer in the Thompson and WDM6 microphysics schemes are essentially dominated by one size bin (Figs. 13g,i). The Thompson scheme artificially increases the number-weighted mean fall speed as a strategy to reduce excessive size sorting (M15). M15 was unable to pinpoint a reason for the WDM6 scheme's proclivity for small raindrops, but their results were consistent with the WDM6's rain distribution in this study.

The relative frequency maxima for the NSSL and Thompson schemes in the smallest bin (Figs. 13e,g) at the low levels appears to be the result of small raindrops forming from autoconversion in the presence of low-level clouds, exhibited by the small D_{mr} near the updrafts seen in Fig. 8. Finally, the Morrison, NSSL, and Thompson schemes produce a secondary area of relative frequency above the melting level (Figs. 13a,e,g). Most of these small drops are likely a result of the updraft carrying supercooled water into upper levels, as the majority of rain at these levels is located near the updrafts. This signal is distinctly absent in the MY2 scheme (Fig. 13c). This is not indicative of a lack of supercooled raindrops, but rather a broad distribution of drops at each level with qualitatively smaller coverage than other schemes (not shown). The WDM6 scheme shows a continuous maximum in the smallest bin extending above the melting layer, similar to the signals at low levels and above the melting layer previously discussed (Fig. 13i). Drops above the melting level are concentrated around the updraft and drops below the melting level could be the result of autoconversion, which is consistent with the other microphysics schemes that exhibit these signals. In any case, the large relative frequency in the smallest D_{mr} bin (Fig. 13i) betrays a distinct bias toward small drops in the WDM6 scheme as compared with the other schemes.

b. Properties of frozen hydrometeors

Graupel and hail CFADs (Figs. 13 and 14) are produced as in section 4a. In the graupel CFADs, several

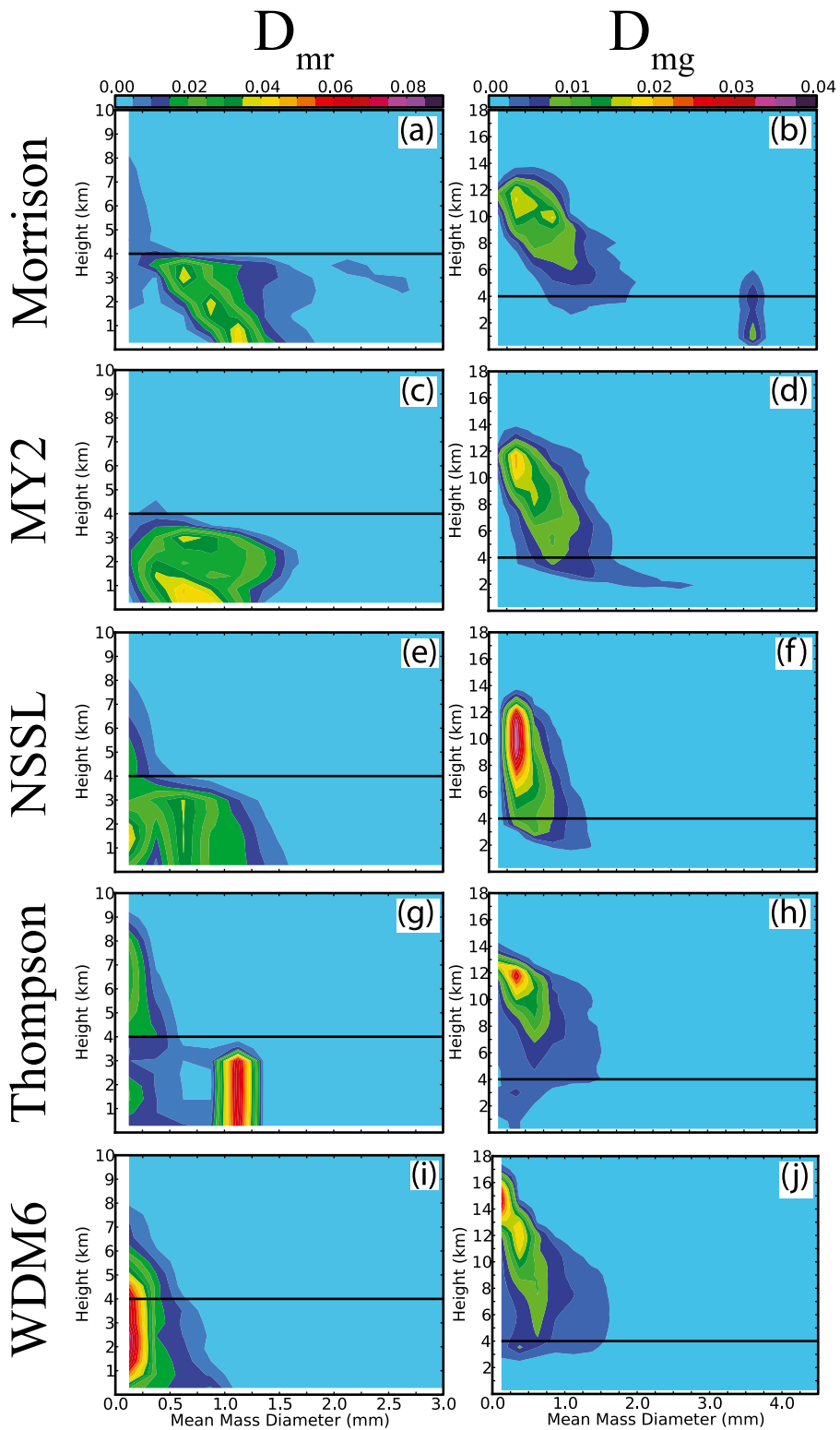


FIG. 13. Rain and graupel CFADs, shown in relation to both D_{mr} and D_{mg} , and height for the (a),(b) Morrison; (c),(d) MY2; (e),(f) NSSL; and (g),(h) Thompson schemes at $t = 100$ min; and the (i),(j) WDM6 scheme at $t = 120$ min. The approximate melting level is shown at 4 km by horizontal black lines.

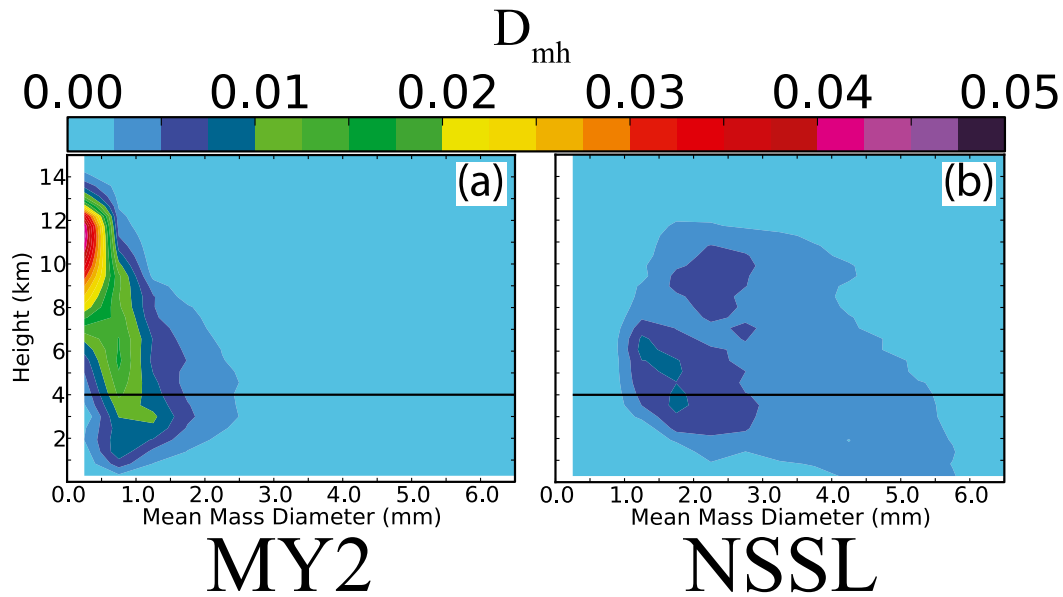


FIG. 14. Hail CFADs, shown in relation to D_{mh} and height for the (a) MY2 and (b) NSSL schemes at $t = 100$ min. The approximate melting level is shown at 4 km by horizontal black lines.

differences are present among the different microphysics schemes. Interestingly, there is a maximum in relative frequency near the surface in the 3.5–3.75-mm D_{mg} bin (Fig. 13b) in the Morrison scheme that extends vertically to approximately 6 km, and is actually connected to the maximum at lower diameters (which can be seen with finer contour intervals). This maximum is likely due to graupel reaching the maximum size threshold in the scheme, since D_{mg} rapidly increases with progressively lower model heights in the Morrison CFAD due to excessive size sorting (Fig. 13b). Excessive size sorting can also be seen in the MY2 scheme, with D_{mg} rapidly increasing near the surface (Fig. 13d). Like the rain PSDs, the shape parameter α is 0 for the graupel PSDs in these schemes, which is likely responsible for the excessive size sorting. In the NSSL scheme (Fig. 13f), D_{mg} does increase with gradually lower model heights but much less than the Morrison and MY2 schemes, likely because of the N_t modification discussed in section 4a. In the Thompson and WDM6 schemes (Figs. 13h,j), D_{mg} weakly increases above the melting layer with progressively lower model heights. The graupel distribution also gets wider at lower heights for both schemes. This is because 1M schemes do not allow size sorting, so little size variation is found with height. The weak D_{mg} increase is solely due to increasing graupel mass. This helps explain why the Thompson and WDM6 schemes were unable to simulate a Z_{DR} arc, because this signature might be influenced more by the size sorting of rimed ice (D14). Graupel only reaches the lowest model level with noticeable relative frequency in the Morrison

and Thompson schemes (Figs. 13b,h) where it has high diagnosed water fraction. This helps explain why graupel-only schemes are unable to reproduce the hail signature, because small- to medium-sized wet graupel (which is oblate) would actually increase Z_{DR} .

The greatest difference between the hail CFADs with the MY2 and NSSL schemes is the magnitude of the relative frequencies. The greatest range of magnitudes in the NSSL scheme is 0.0075–0.01 (Fig. 14b), while maximum magnitudes in the MY2 scheme range from 0.0425 to 0.045 (Fig. 14a). The most likely explanation for this is that frozen rain is included in the hail category in the MY2 scheme, while frozen rain is included in the graupel category in the NSSL scheme. In other words, the main source of hail is frozen rain in the MY2 scheme, while the main source of hail in the NSSL scheme is graupel undergoing wet growth, which explains the dominant hail size difference between the two schemes. The NSSL scheme, by virtue of its prognostic graupel density, allows the assignment of high-density frozen rain in the graupel category (Mansell et al. 2010). Much larger hail is found in the NSSL CFAD near the surface than the MY2 CFAD (Fig. 14). This is consistent with results from section 3d, where large dry hail is able to form a hail signature in the NSSL scheme.

5. Summary and discussion

In this paper, we performed idealized supercell storm simulations with several two-moment (2M) microphysics schemes available in the WRF Model. We aimed to

1) determine how well each microphysics scheme reproduces unique polarimetric signatures in supercell storms, 2) relate the presence and relative magnitude of these signatures to the characteristics of the hydrometeors produced by the microphysics scheme and 3) further investigate the behaviors and properties of each microphysics scheme through hydrometeor relative frequency distributions. Five fully or partially 2M schemes in the WRF Model were evaluated, and polarimetric variables were calculated from the model output using an enhanced polarimetric radar simulator. Those five schemes were the Morrison, Milbrandt–Yau, NSSL, Thompson, and WDM6 schemes.

Here we summarize results and their corresponding conclusions for the microphysics schemes evaluated in the supercell storm simulations:

- 1) Each scheme is able to produce the Z_{DR} and K_{DP} columns, although the intensity of the columns varies significantly among the schemes. The Thompson scheme presents the strongest Z_{DR} and K_{DP} columns because of relatively larger graupel size with high liquid water content. The NSSL scheme produces a relatively weak Z_{DR} column because it produces hail that is generally too large to hold much water before it sheds and likely appears spherical to radar since it has the potential to tumble. The MY2 scheme produces the weakest K_{DP} column because of its smallest q_r values among schemes.
- 2) The Morrison, MY2, and NSSL schemes are able to simulate a Z_{DR} arc, with the NSSL scheme producing the most realistic signature. This is allowed by the 2M nature of their respective rimed-ice categories. The Morrison scheme produces higher Z_{DR} values in the arc than the other schemes due to relatively larger raindrops produced by the scheme. The Thompson and WDM6 schemes, which contain 1M rimed-ice categories, are unable to replicate a Z_{DR} arc, most likely because of the lack of rimed-ice size sorting.
- 3) Each microphysics scheme, except for the Thompson scheme, is able to simulate an enhanced, ringlike (full or half) midlevel Z_{DR} signature. The major contributors to the midlevel Z_{DR} ring are small- to medium-sized wet rimed-ice particles along with relatively large raindrops, which have oblate shapes. However, small graupel particles contribute to the WDM6 scheme having the lowest overall Z_{DR} values. All but the WDM6 scheme simulate a reduced ρ_{HV} area around the updraft, due to small graupel in the scheme that does not encounter the resonance effect. The NSSL scheme reduces ρ_{HV} the most, as partially wet hail in the scheme is likely dominated by the resonance effect.
- 4) The hail signature in the forward-flank downdraft simulated in this study relies on the presence of large, dry hail at the surface, which reduces Z_{DR} . Microphysics schemes that only contain a graupel-like rimed-ice category fail to reproduce this signature. The graupel particles that do reach the lowest model level in these schemes are small to medium sized with high water fraction, which increase Z_{DR} . In fact, only the NSSL scheme is able to reproduce this signature, due to large dry hail reaching the lowest model level. Hailstones near the surface in the MY2 scheme are small to medium sized and wet, and thus fail to simulate the hail signature.
- 5) Each scheme is able to simulate the K_{DP} foot near the surface. The Thompson scheme produces the strongest K_{DP} foot primarily due to high liquid water mass residing on melting graupel. The Morrison, MY2, and WDM6 schemes produce the weakest K_{DP} foot, due to low liquid water mass in the MY2 scheme and relatively smaller drops in the Morrison and WDM6 schemes in the vicinity of this signature.
- 6) Excessive size sorting of raindrops near the surface is evident in the Morrison and MY2 rain CFADs, while the other schemes display more gradual size sorting. This is primarily due to the constant shape parameter of zero for the rain PSDs in the Morrison and MY2 schemes, while the other schemes have strategies to inhibit size sorting (NSSL, Thompson), or are just dominated by small drops (WDM6). Particularly, the much larger drops present in the Morrison rain CFAD as a result of excessive size sorting help explain the largest Z_{DR} values in the Z_{DR} arc compared to the other schemes.
- 7) Graupel CFADs exhibit similar size-sorting characteristics in the Morrison, MY2, and NSSL schemes as in the rain CFADs. The Thompson and WDM6 graupel CFADs show a distinct lack of size sorting due to the 1M nature of the graupel category, which helps explain why the schemes were unable to simulate a Z_{DR} arc due to the signature's possible dependence on rimed-ice size sorting. The graupel CFADs also show that among the graupel-only schemes, no large dry graupel reached the lowest model level, which helps explain why the graupel-only schemes were unable to simulate the hail signature. The much larger hail sizes near the surface in the NSSL CFAD help explain the ability of the scheme to replicate the hail signature, as smaller hail in the MY2 CFAD is simulated as wet.

The ability of microphysical schemes to reproduce observed polarimetric signatures is critical for direct assimilation of polarimetric measurements

into convective-scale NWP models. If the model is unable to produce the information carried by observations, direct assimilation of such observations is unlikely to produce correct impacts as assimilation of such observations aims to reduce the difference between the simulated and observed information. For example, when graupel never reaches the ground in a certain microphysics scheme due to low density and slow terminal velocity assumptions, assimilating the hail signature will likely remove rain from the area and result in a hole in surface precipitation. Studies such as the current one can give us an idea as to whether or not a certain microphysics scheme needs improvement in particular aspects to allow for successful assimilation of polarimetric data. Although this study is able to relate the presence of unique supercell polarimetric signatures to the hydrometeor PSD characteristics, additional studies comparing microphysics schemes for different types of convective systems are needed. These will not only help users choose suitable schemes for their purposes, but also help developers to improve and identify weaknesses of their schemes.

One area in particular that deserves more attention is the parameterization of large rimed ice. In our study, the two signatures that appear most sensitive to rimed-ice parameterizations are the Z_{DR} arc and the hail signature in the forward-flank downdraft. In regard to the Z_{DR} arc, this study found that the rimed-ice category needs to be at least 2M in order to replicate size sorting, which agrees with the results of D14. In regard to the hail signature, the most important differences are with schemes with only a graupel-like rimed-ice category versus schemes with an additional hail-like rimed-ice category. Indeed, schemes with only a graupel-like rimed-ice category are unable to replicate this signature. This has significant implications for the design of microphysics schemes with respect to the treatment of graupel and hail processes.

Comparing the schemes that contain an additional hail category, the NSSL scheme is able to produce a much more prominent hail signature than the MY2 scheme. While the exact reason for this is not clear, it is worth reiterating the differences between the treatment of the rimed-ice categories in these two schemes. First, the MY2 scheme employs a fixed bulk density, while the NSSL scheme predicts graupel particle volume (from which graupel density can be calculated). Second, and related to the first, the NSSL scheme assigns (high density) frozen drops to the graupel category; because graupel density is prognosed, this results in relatively high-density graupel that can later grow into hail. In contrast, the MY2 scheme places frozen drops into the (fixed high density) hail category, presumably since the

graupel density is fixed at a relatively low value. As seen in the frequency plots in section 4, hail is much larger in the NSSL scheme than the MY2 scheme, presumably because hail initiates from graupel that has already had time to grow in the NSSL scheme rather than the much smaller frozen drops in the MY2 scheme. These differences in the treatment of rimed-ice processes appear to allow hail to grow larger in the NSSL scheme and produce a much more prominent hail signature. The impact of rimed-ice parameterization on polarimetric signatures is clearly complex and requires further study.

Acknowledgments. This research was supported by a research grant of “Development of a Polarimetric Radar Data Simulator for Local Forecasting Model” by the Korea Meteorological Administration. Further support was provided by NSF Grants AGS-1046171 and AGS-1261776. We also thank three anonymous reviewers who greatly improved the quality of this manuscript.

REFERENCES

- Brandes, E. A., J. Vivekanandan, J. D. Tuttle, and C. J. Kessinger, 1995: A study of thunderstorm microphysics with multiparameter radar and aircraft observations. *Mon. Wea. Rev.*, **123**, 3129–3143, doi:10.1175/1520-0493(1995)123<3129:ASOTMW>2.0.CO;2.
- , G. Zhang, and J. Vivekanandan, 2002: Experiments in rainfall estimation with a polarimetric radar in a subtropical environment. *J. Appl. Meteor.*, **41**, 674–685, doi:10.1175/1520-0450(2002)041<0674:EIREWA>2.0.CO;2.
- Cintineo, R., J. A. Otkin, M. Xue, and F. Kong, 2014: Evaluating the performance of planetary boundary layer and cloud microphysical parameterization schemes in convection-permitting ensemble forecasts using synthetic GOES-13 satellite observations. *Mon. Wea. Rev.*, **142**, 163–182, doi:10.1175/MWR-D-13-00143.1.
- Cohard, J.-M., and J.-P. Pinty, 2000: A comprehensive two-moment warm microphysical bulk scheme. I: Description and tests. *Quart. J. Roy. Meteor. Soc.*, **126**, 1815–1842, doi:10.1256/smsqj.56613.
- Conway, J. W., and D. S. Zrnić, 1993: A study of embryo production and hail growth using dual-Doppler and multiparameter radars. *Mon. Wea. Rev.*, **121**, 2511–2528, doi:10.1175/1520-0493(1993)121<2511:ASOEP A>2.0.CO;2.
- Cotton, W. R., G. J. Tripoli, R. M. Rauber, and E. A. Mulvihill, 1986: Numerical simulation of the effects of varying ice crystal nucleation rates and aggregation processes on orographic snowfall. *J. Climate Appl. Meteor.*, **25**, 1658–1680, doi:10.1175/1520-0450(1986)025<1658:NSOTEO>2.0.CO;2.
- Dawson, D. T., II, M. Xue, J. A. Milbrandt, and M. K. Yau, 2010: Comparison of evaporation and cold pool development between single-moment and multimoment bulk microphysics schemes in idealized simulations of tornadic thunderstorms. *Mon. Wea. Rev.*, **138**, 1152–1171, doi:10.1175/2009MWR2956.1.
- , L. J. Wicker, E. R. Mansell, and R. L. Tanamachi, 2012: Impact of the environmental low-level wind profile on ensemble forecasts of the 4 May 2007 Greensburg, Kansas,

- tornadic storm and associated mesocyclones. *Mon. Wea. Rev.*, **140**, 696–716, doi:10.1175/MWR-D-11-00008.1.
- , E. R. Mansell, Y. Jung, L. J. Wicker, M. R. Kumjian, and M. Xue, 2014: Low-level ZDR signatures in supercell forward flanks: The role of size sorting and melting of hail. *J. Atmos. Sci.*, **71**, 276–299, doi:10.1175/JAS-D-13-0118.1.
- , —, and M. R. Kumjian, 2015a: Does wind shear cause hydrometeor size sorting? *J. Atmos. Sci.*, **72**, 340–348, doi:10.1175/JAS-D-14-0084.1.
- , M. Xue, J. A. Milbrandt, and A. Shapiro, 2015b: Sensitivity of real-data simulations of the 3 May 1999 Oklahoma City tornadic supercell and associated tornadoes to multimoment microphysics. Part I: Storm- and tornado-scale numerical forecasts. *Mon. Wea. Rev.*, **143**, 2241–2265, doi:10.1175/MWR-D-14-00279.1.
- Ferrier, B. S., 1994: A double-moment multiple-phase four-class bulk ice scheme. Part I: Description. *J. Atmos. Sci.*, **51**, 249–280, doi:10.1175/1520-0469(1994)051<0249:ADMMPF>2.0.CO;2.
- Field, P. R., R. J. Hogan, P. R. A. Brown, A. J. Illingworth, T. W. Choullarton, and R. J. Cotton, 2005: Parameterization of ice-particle size distributions for mid-latitude stratiform cloud. *Quart. J. Roy. Meteor. Soc.*, **131**, 1997–2017, doi:10.1256/qj.04.134.
- Hendry, A., and G. C. McCormick, 1976: Radar observations of the alignment of precipitation particles by electrostatic fields in thunderstorms. *J. Geophys. Res.*, **81**, 5353–5357, doi:10.1029/JC081i030p05353.
- Hong, S.-Y., and J.-O. J. Lim, 2006: The WRF single-moment 6-class microphysics scheme (WSM6). *J. Korean Meteor. Soc.*, **42**, 129–151.
- Hubbert, J., V. N. Bringi, L. D. Carey, and S. Bolen, 1998: CSU-CHILL polarimetric radar measurements from a severe hail storm in eastern Colorado. *J. Appl. Meteor.*, **37**, 749–775, doi:10.1175/1520-0450(1998)037<0749:CCPRMF>2.0.CO;2.
- Illingworth, A. J., J. W. F. Goddard, and S. M. Cherry, 1987: Polarization radar studies of precipitation development in convective storms. *Quart. J. Roy. Meteor. Soc.*, **113**, 469–489, doi:10.1002/qj.49711347604.
- Jung, Y., G. Zhang, and M. Xue, 2008: Assimilation of simulated polarimetric radar data for a convective storm using the ensemble Kalman filter. Part I: Observation operators for reflectivity and polarimetric variables. *Mon. Wea. Rev.*, **136**, 2228–2245, doi:10.1175/2007MWR2083.1.
- , M. Xue, and G. Zhang, 2010a: Simulations of polarimetric radar signatures of a supercell storm using a two-moment bulk microphysics scheme. *J. Appl. Meteor. Climatol.*, **49**, 146–163, doi:10.1175/2009JAMC2178.1.
- , —, and —, 2010b: Simultaneous estimation of microphysical parameters and the atmospheric state using simulated polarimetric radar data and an ensemble Kalman filter in the presence of an observation operator error. *Mon. Wea. Rev.*, **138**, 539–562, doi:10.1175/2009MWR2748.1.
- , —, and M. Tong, 2012: Ensemble Kalman filter analyses of the 29–30 May 2004 Oklahoma tornadic thunderstorm using one- and two-moment bulk microphysics schemes, with verification against polarimetric radar data. *Mon. Wea. Rev.*, **140**, 1457–1475, doi:10.1175/MWR-D-11-00032.1.
- Kessler, E., 1969: *On the Distribution and Continuity of Water Substance in Atmospheric Circulations*. *Meteor. Monogr.*, No. 32, Amer. Meteor. Soc., 84 pp.
- Khain, A., A. Pokrovsky, M. Pinsky, A. Seifert, and V. Phillips, 2004: Simulation of effects of atmospheric aerosols on deep turbulent convective clouds using a spectral microphysics mixed-phase cumulus cloud model. Part I: Model description and possible applications. *J. Atmos. Sci.*, **61**, 2963–2982, doi:10.1175/JAS-3350.1.
- Klemp, J. B., 1987: Dynamics of tornadic thunderstorms. *Annu. Rev. Fluid Mech.*, **19**, 369–402, doi:10.1146/annurev.fl.19.010187.002101.
- , and R. B. Wilhelmson, 1978: Simulations of right- and left-moving storms produced through storm splitting. *J. Atmos. Sci.*, **35**, 1097–1110, doi:10.1175/1520-0469(1978)035<1097:SORALM>2.0.CO;2.
- Knight, C. A., and N. C. Knight, 1970: The falling behavior of hailstones. *J. Atmos. Sci.*, **27**, 672–681, doi:10.1175/1520-0469(1970)027<0672:TFBOH>2.0.CO;2.
- Knight, N. C., 1986: Hailstone shape factor and its relation to radar interpretation of hail. *J. Climate Appl. Meteor.*, **25**, 1956–1958, doi:10.1175/1520-0450(1986)025<1956:HSFAIR>2.0.CO;2.
- Kogan, Y. L., and A. Belochitski, 2012: Parameterization of cloud microphysics based on full integral moments. *J. Atmos. Sci.*, **69**, 2229–2242, doi:10.1175/JAS-D-11-0268.1.
- Kong, F., and Coauthors, 2007: Preliminary analysis on the real-time storm-scale ensemble forecasts produced as a part of the NOAA hazardous weather testbed 2007 spring experiment. *22nd Conf. on Weather Analysis and Forecasting/18th Conf. on Numerical Weather Prediction*, Park City, UT, Amer. Meteor. Soc., 3B.2. [Available online from https://ams.confex.com/ams/22WAF18NWP/techprogram/paper_124667.htm.]
- , and Coauthors, 2014: CAPS storm-scale ensemble forecasting system: Impact of IC and LBC perturbations. *26th Conf. on Weather Analysis and Forecasting/22nd Conf. on Numerical Weather Prediction*, Atlanta, GA, Amer. Meteor. Soc., 119. [Available online from <https://ams.confex.com/ams/94Annual/webprogram/Paper234762.html>.]
- Kumjian, M. R., and A. V. Ryzhkov, 2008: Polarimetric signatures in supercell thunderstorms. *J. Appl. Meteor. Climatol.*, **47**, 1940–1961, doi:10.1175/2007JAMC1874.1.
- , and —, 2009: Storm-relative helicity revealed from polarimetric radar measurements. *J. Atmos. Sci.*, **66**, 667–685, doi:10.1175/2008JAS2815.1.
- , and —, 2012: The impact of size sorting on the polarimetric radar variables. *J. Atmos. Sci.*, **69**, 2042–2060, doi:10.1175/JAS-D-11-0125.1.
- Lim, K.-S. S., and S.-Y. Hong, 2010: Development of an effective double-moment cloud microphysics scheme with prognostic cloud condensation nuclei (CCN) for weather and climate models. *Mon. Wea. Rev.*, **138**, 1587–1612, doi:10.1175/2009MWR2968.1.
- Lin, Y.-L., R. D. Farley, and H. D. Orville, 1983: Bulk parameterization of the snow field in a cloud model. *J. Climate Appl. Meteor.*, **22**, 1065–1092, doi:10.1175/1520-0450(1983)022<1065:BPOTSF>2.0.CO;2.
- Loney, M. L., D. S. Zrnić, J. M. Straka, and A. V. Ryzhkov, 2002: Enhanced polarimetric radar signatures above the melting level in a supercell storm. *J. Appl. Meteor.*, **41**, 1179–1194, doi:10.1175/1520-0450(2002)041<1179:EPRSAT>2.0.CO;2.
- Mansell, E. R., 2010: On sedimentation and advection in multimoment bulk microphysics. *J. Atmos. Sci.*, **67**, 3084–3094, doi:10.1175/2010JAS3341.1.
- , and C. L. Ziegler, 2013: Aerosol effects on simulated storm electrification and precipitation in a two-moment bulk microphysics model. *J. Atmos. Sci.*, **70**, 2032–2050, doi:10.1175/JAS-D-12-0264.1.
- , —, and E. C. Bruning, 2010: Simulated electrification of a small thunderstorm with two-moment bulk microphysics. *J. Atmos. Sci.*, **67**, 171–194, doi:10.1175/2009JAS2965.1.

- Meyers, M. P., R. L. Walko, J. Y. Harrington, and W. R. Cotton, 1997: New RAMS cloud microphysics parameterization. Part II: The two-moment scheme. *Atmos. Res.*, **45**, 3–39, doi:10.1016/S0169-8095(97)00018-5.
- Milbrandt, J. A., and M. K. Yau, 2005a: A multimoment bulk microphysics parameterization. Part I: Analysis of the role of the spectral shape parameter. *J. Atmos. Sci.*, **62**, 3051–3064, doi:10.1175/JAS3534.1.
- , and —, 2005b: A multimoment bulk microphysics parameterization. Part II: A proposed three-moment closure and scheme description. *J. Atmos. Sci.*, **62**, 3065–3081, doi:10.1175/JAS3535.1.
- , and —, 2006: A multimoment bulk microphysics parameterization. Part IV: Sensitivity experiments. *J. Atmos. Sci.*, **63**, 3137–3159, doi:10.1175/JAS3817.1.
- , and R. McTaggart-Cowan, 2010: Sedimentation-induced errors in bulk microphysics schemes. *J. Atmos. Sci.*, **67**, 3931–3948, doi:10.1175/2010JAS3541.1.
- Morrison, H., and J. Milbrandt, 2011: Comparison of two-moment bulk microphysics schemes in idealized supercell thunderstorm simulations. *Mon. Wea. Rev.*, **139**, 1103–1130, doi:10.1175/2010MWR3433.1.
- , G. Thompson, and V. Tatarskii, 2009: Impact of cloud microphysics on the development of trailing stratiform precipitation in a simulated squall line: Comparison of one- and two-moment schemes. *Mon. Wea. Rev.*, **137**, 991–1007, doi:10.1175/2008MWR2556.1.
- , J. A. Milbrandt, G. H. Bryan, K. Ikeda, S. A. Tessendorf, and G. Thompson, 2015: Parameterization of cloud microphysics based on the prediction of bulk ice particle properties. Part II: Case study comparisons with observations and other schemes. *J. Atmos. Sci.*, **72**, 312–339, doi:10.1175/JAS-D-14-0066.1.
- Potvin, C. K., L. J. Wicker, M. I. Biggerstaff, D. Betten, and A. Shapiro, 2013: Comparison between dual-Doppler and EnKF storm-scale wind analyses: The 29–30 May 2004 Geary, Oklahoma, supercell thunderstorm. *Mon. Wea. Rev.*, **141**, 1612–1628, doi:10.1175/MWR-D-12-00308.1.
- Putnam, B. J., M. Xue, Y. Jung, N. A. Snook, and G. Zhang, 2014: The analysis and prediction of microphysical states and polarimetric radar variables in a mesoscale convective system using double-moment microphysics, multinet radar data, and the ensemble Kalman filter. *Mon. Wea. Rev.*, **142**, 141–162, doi:10.1175/MWR-D-13-00042.1.
- Rasmussen, R. M., and A. J. Heymsfield, 1987: Melting and shedding of graupel and hail. Part I: Model physics. *J. Atmos. Sci.*, **44**, 2754–2763, doi:10.1175/1520-0469(1987)044<2754:MASOGA>2.0.CO;2.
- , V. Levizzani, and H. R. Pruppacher, 1984: A wind tunnel and theoretical study on the melting behavior of atmospheric ice particles: III. Experiment and theory for spherical ice particles of radius $> 500 \mu\text{m}$. *J. Atmos. Sci.*, **41**, 381–388, doi:10.1175/1520-0469(1984)041<0381:AWTATS>2.0.CO;2.
- Romine, G. S., D. W. Burgess, and R. B. Wilhelmson, 2008: A dual-polarization-radar-based assessment of the 8 May 2003 Oklahoma City area tornadic supercell. *Mon. Wea. Rev.*, **136**, 2849–2870, doi:10.1175/2008MWR2330.1.
- Rotunno, R., and J. B. Klemp, 1982: The influence of the shear-induced pressure gradient on thunderstorm motion. *Mon. Wea. Rev.*, **110**, 136–151, doi:10.1175/1520-0493(1982)110<0136:TIOTSI>2.0.CO;2.
- Rutledge, S. A., and P. V. Hobbs, 1983: The mesoscale and microscale structure and organization of clouds and precipitation in midlatitude cyclones. VIII: A model for the “seeder-feeder” process in warm-frontal rainbands. *J. Atmos. Sci.*, **40**, 1185–1206, doi:10.1175/1520-0469(1983)040<1185:TMAMSA>2.0.CO;2.
- Ryzhkov, A. V., T. J. Schuur, D. W. Burgess, and D. S. Zrnić, 2005: Polarimetric tornado detection. *J. Appl. Meteor.*, **44**, 557–570, doi:10.1175/JAM2235.1.
- Schuur, T. J., A. V. Ryzhkov, P. L. Heinselman, D. S. Zrnić, D. W. Burgess, and K. A. Scharfenberg, 2003: Observations and classification of echoes with the polarimetric WSR-88D radar. NOAA/National Severe Storms Laboratory Rep., 46 pp. [Available online from http://www.cimms.ou.edu/~schuur/jpole/JPOLE_HCA_report_pdf.pdf.]
- Skamarock, W. C., and Coauthors, 2008: A description of the Advanced Research WRF version 3. NCAR Tech. Note NCAR/TN-475+STR, 113 pp., doi:10.5065/D68S4MVH.
- Straka, J. M., and E. R. Mansell, 2005: A bulk microphysics parameterization with multiple ice precipitation categories. *J. Appl. Meteor.*, **44**, 445–466, doi:10.1175/JAM2211.1.
- , D. S. Zrnić, and A. V. Ryzhkov, 2000: Bulk hydrometeor classification and quantification using polarimetric radar data: Synthesis of relations. *J. Appl. Meteor.*, **39**, 1341–1372, doi:10.1175/1520-0450(2000)039<1341:BHCAQU>2.0.CO;2.
- Tao, W.-K., and J. Simpson, 1993: Goddard cumulus ensemble model. Part I: Model description. *Terr. Atmos. Oceanic Sci.*, **4**, 35–72.
- Thompson, G., P. R. Field, R. M. Rasmussen, and W. D. Hall, 2008: Explicit forecasts of winter precipitation using an improved bulk microphysics scheme. Part II: Implementation of a new snow parameterization. *Mon. Wea. Rev.*, **136**, 5095–5115, doi:10.1175/2008MWR2387.1.
- Thwaites, S., J. N. Carras, and W. C. Macklin, 1977: The aerodynamics of oblate hailstones. *Quart. J. Roy. Meteor. Soc.*, **103**, 803–808, doi:10.1002/qj.49710343819.
- Van Weverberg, K., A. M. Vogelmann, H. Morrison, and J. A. Milbrandt, 2012: Sensitivity of idealized squall-line simulations to the level of complexity used in two-moment bulk microphysics schemes. *Mon. Wea. Rev.*, **140**, 1883–1907, doi:10.1175/MWR-D-11-00120.1.
- Vivekanandan, J., W. M. Adams, and V. N. Bringi, 1991: Rigorous approach to polarimetric radar modeling of hydrometeor orientation distributions. *J. Appl. Meteor.*, **30**, 1053–1063, doi:10.1175/1520-0450(1991)030<1053:RATPRM>2.0.CO;2.
- Wacker, U., and A. Seifert, 2001: Evolution of rain water profiles resulting from pure sedimentation: Spectral vs. parameterized description. *Atmos. Res.*, **58**, 19–39, doi:10.1016/S0169-8095(01)00081-3.
- Waterman, P. C., 1969: Scattering by dielectric obstacles. *Alta Freq.*, **38**, 348–352.
- Weisman, M. L., and J. B. Klemp, 1982: The dependence of numerically simulated convective storms on vertical wind shear and buoyancy. *Mon. Wea. Rev.*, **110**, 504–520, doi:10.1175/1520-0493(1982)110<0504:TDonSC>2.0.CO;2.
- , W. C. Skamarock, and J. B. Klemp, 1997: The resolution dependence of explicitly modeled convective systems. *Mon. Wea. Rev.*, **125**, 527–548, doi:10.1175/1520-0493(1997)125<0527:TRDOEM>2.0.CO;2.
- Xue, M., and Coauthors, 2007: CAPS realtime storm-scale ensemble and high-resolution forecasts as part of the NOAA Hazardous Weather Testbed 2007 spring experiment. *22nd Conf. on Weather Analysis and Forecasting/18th Conf. on Numerical Weather Prediction*, Park City, UT, Amer. Meteor. Soc., 3B.1. [Available online from https://ams.confex.com/ams/22WAF18NWP/techprogram/paper_124587.htm.]

- , and Coauthors, 2008: CAPS realtime storm-scale ensemble and high-resolution forecasts as part of the NOAA Hazardous Weather Testbed 2008 Spring Experiment. *24th Conf. on Several Local Storms*, Savannah, GA, Amer. Meteor. Soc., 12.2. [Available online from https://ams.confex.com/ams/24SLS/techprogram/paper_142036.htm.]
- , and Coauthors, 2010a: CAPS realtime storm-scale ensemble and high-resolution forecasts for the NOAA Hazardous Weather Testbed 2010 spring experiment. *25th Conf. on Severe Local Storms*, Denver, CO, Amer. Meteor. Soc., 7B.3. [Available online from https://ams.confex.com/ams/25SLS/techprogram/paper_176056.htm.]
- , Y. Jung, and G. Zhang, 2010b: State estimation of convective storms with a two-moment microphysics scheme and an ensemble Kalman filter: Experiments with simulated radar data. *Quart. J. Roy. Meteor. Soc.*, **136**, 685–700, doi:10.1002/qj.593.
- Yuter, S. E., and R. A. Houze Jr., 1995: Three-dimensional kinematic and microphysical evolution of Florida cumulonimbus. Part II: Frequency distributions of vertical velocity, reflectivity, and differential reflectivity. *Mon. Wea. Rev.*, **123**, 1941–1963, doi:10.1175/1520-0493(1995)123<1941:TDKAME>2.0.CO;2.
- Zhang, G., J. Vivekanandan, and E. Brandes, 2001: A method for estimating rain rate and drop size distribution from polarimetric radar measurements. *IEEE Trans. Geosci. Remote Sens.*, **39**, 830–841, doi:10.1109/36.917906.
- Ziegler, C. L., 1985: Retrieval of thermal and microphysical variables in observed convective storms. Part I: Model development and preliminary testing. *J. Atmos. Sci.*, **42**, 1487–1509, doi:10.1175/1520-0469(1985)042<1487:ROTAMV>2.0.CO;2.